

國立臺灣大學 理學院物理學研究所

碩士學位論文

Graduate Institute of Physics

College of Science

National Taiwan University

Master Thesis

在KOTO實驗中尋找無質量暗光子： $K_L^0 \rightarrow \gamma\bar{\gamma}$

Search for a massless dark photon in $K_L^0 \rightarrow \gamma\bar{\gamma}$ at the
KOTO Experiment

吳桐

Tong Wu

指導教授：熊怡 教授

Advisor: Yee Bob Hsiung, Ph.D.

中華民國113年8月

August 2024

NATIONAL TAIWAN UNIVERSITY

MASTER THESIS

**Search for a massless dark photon in
 $K_L^0 \rightarrow \gamma\bar{\gamma}$ at the KOTO Experiment**

Author:

Tong Wu

Supervisor:

Dr. Yee Bob HSIUNG



July 28, 2024

© 2024, by Tong Wu
tong@hep1.phys.ntu.edu.tw



ALL RIGHTS RESERVED

Acknowledgements

Thanks all

DRAFT

中文摘要

一二三

三二一

關鍵詞：暗光子、新物理。

DRAFT

Abstract

This thesis presents the search for the massless dark photon ($\bar{\gamma}$) in the $K_L^0 \rightarrow \gamma\bar{\gamma}$ decay at the J-PARC KOTO experiment, based on the special run data collected in 2020.

Distinguished from the massive dark photon, the massless one does not directly mix with the ordinary photon but could interact with Standard Model (SM) particles through direct coupling to quarks. Some theoretical models propose that the branching ratio (\mathcal{BR}) of the $K_L^0 \rightarrow \gamma\bar{\gamma}$ decay could reach up to $\mathcal{O}(10^{-3})$.

The number of K_L^0 decays that had been collected in the special run is estimated to be $(1.29 \pm 0.02) \times 10^{10}$. The single event sensitivity is calculated to be $(2.91 \pm 0.02_{stat.} \pm 0.30_{syst.}) \times 10^{-8}$. The total background level prediction is $(12.66 \pm 4.42_{stat.} \pm 2.13_{syst.})$ with the agreement from the side-band region. We uncovered the blind region and observed 13 events. The Feldman-Cousins method is used to calculate the upper limit of the $K_L^0 \rightarrow \gamma\bar{\gamma}$ branching ratio to be $< 3.47 \times 10^{-7}$ (90% C.L.).

Keywords: Dark Photon, beyond Standard Model.

Contents

Approval	i
Acknowledgements	iii
中文摘要	v
Abstract	vii
Contents	ix
List of Figures	xiii
List of Tables	xvii
1 Introduction	1
1.1 Dark Matter and Dark Photons	1
1.2 Theoretical Predictions	1
1.3 Basic Strategy of the $K_L^0 \rightarrow \gamma\bar{\gamma}$ Search	2
1.3.1 Signal Identification	2
1.3.2 Major Background Sources	2
1.4 Thesis Overview	3
2 KOTO Experiment	5
2.1 J-PARC and Proton Beamline	5
2.2 K_L^0 Beamline	6
2.3 Detectors	7
2.3.1 CsI	8
2.3.2 Charge Veto Counter	10
2.3.3 Barrel Veto Counter	10
2.4 Data Acquisition System	12
3 Event Reconstruction	13
3.1 Photon Cluster Finding	13
3.2 Reconstruction of π^0	15
3.3 Reconstruction of Decays	16
3.3.1 Reconstruction of $K_L^0 \rightarrow 3\pi^0$	17
3.3.2 Reconstruction of $K_L^0 \rightarrow \gamma\bar{\gamma}$	18
3.3.3 Correction for Energy and Position of Photon Clusters	18
3.4 Veto Hit Reconstruction	20
3.4.1 Barrel Veto Counters	21

3.4.2	CsI Calorimeter	22
4	Monte Carlo Simulation	25
4.1	GEANT4 toolkit	25
4.2	Detector Response	26
4.3	Pulse Simulation	26
4.4	K_L^0 Generation	26
4.4.1	Beamline Simulation	26
4.4.2	Empirical K_L^0 Spectrum Simulation	27
4.5	Fast Simulation	28
4.6	Accidental Overlay	29
4.7	Neutron background Simulation	30
5	K_L^0 Yield Estimation	31
5.1	Data Set	31
5.2	Event Selections	32
5.2.1	Trigger Cut	32
5.2.2	Photon Selection	32
5.2.3	K_L^0 Selection	34
5.2.4	Veto Cut	36
5.3	Yield Estimation	37
5.3.1	Estimation by $K_L^0 \rightarrow 3\pi^0$ Decays	38
5.4	Summary of K_L^0 Yield Estimation	39
6	Analysis of $K_L \rightarrow \gamma\bar{\gamma}$	43
6.1	Data Set	44
6.2	Basic Strategy of the Single Cluster Study	45
6.2.1	Signal Identification	45
6.2.2	Major Background Sources	45
6.3	Single Cluster Event Selection	46
6.3.1	Trigger Selection	46
6.3.2	Kinematic Cuts	47
6.3.3	Veto Cuts	48
6.4	Background Suppression	50
6.4.1	K_L Decay Background	50
6.4.2	Neutron Background	53
6.5	Single Event Sensitivity	58
6.5.1	Systematic Uncertainty of SES	59
6.6	Additional Background Source Study	59
6.7	Background Level Estimation	61
6.8	Unbind the Signal Region	61
7	Conclusion and Discussion	63

7.1 Discussion for Next Step	64
7.2 Massive Dark Photon Search	64
Bibliography	67

List of Figures

2.1	The entire view of J-PARC. [5]	5
2.2	Illustration of the Hadron Experimental Facility (HEF) at J-PARC.[9] The KL in the Figure indicated the KOTO detector	6
2.3	Structural drawings of the T1 production target [10]. One bar is used for production and the other is a spare.	7
2.4	Schematic diagram of the K_L^0 beamline.[11]	7
2.5	Beamline layout	8
2.6	Schematic diagram of CsI layout.	9
2.7	KOTO detector layout	10
2.8	The Schematic Diagram of Charge Veto Structure.	11
2.9	The Schematic Diagram of Barrel Veto Structure. Figure courtesy of [15].	11
2.10	The architecture of the KOTO DAQ system. [16]	12
3.1	The illustration of the cluster finding process. All the color crystals are the seed crystals, and the crystals with the same color belong to the same cluster. The black crystal is the isolated crystal hit.	14
3.2	Timing boundary for a cluster seed based on the scattered plot of crystal timing versus energy deposit. A Gaussian function is fitted at each energy bin and the boundary is defined by $\mu \pm 5\sigma$, where μ and σ are the Gaussian mean and standard deviation. The orange points indicate the boundary at the associated energy bin. The red curve connects all the points for the interpolation of the boundary value between the points. (Figure courtesy of [15])	15
3.3	The schematic diagram of the $\pi^0 \rightarrow 2\gamma$ decay process.	16
3.4	The schematic diagram of the K_L^0 travel and decay process and geometry relationships	18
3.5	The schematic diagram of the correction of the photon cluster position.	19
3.6	Schematic view of the timings used in the module-veto-timing calculation.	21
3.7	The Schematic diagram of a photon hit with the generated scintillation lights propagating to both directions and captured by PMTs. Figure courtesy of [15]	22
3.8	The Schematic diagram of geometry relationships of the Barrel veto counter.	22
4.1	Beam content at the KOTO detector entrance based on the beamline simulation. Figure courtesy of [15]	27

4.2	The K_L^0 momentum spectrum at the exit of the second collimator. Figure courtesy of [15]	28
4.3	Comparison of K_L^0 beam profile at the exit of the second collimator between the beamline simulation and the empirical model. Figure courtesy of [15]	28
4.4	An example of the accidental overlay on a simulated pulse, subtracting the pedestal. Figure courtesy of [15]	30
5.1	Distribution of the photon selection variables for the $K_L^0 \rightarrow 3\pi^0$ decay. The photon selection cuts are applied except for the variable shown in the plot. The black point shows the data, and the fill histogram shows the Monte Carlo simulation. The red arrow indicates the cut-off value of the variable.	33
5.2	Distribution of the K_L^0 selection variables for the $K_L^0 \rightarrow 3\pi^0$ decay. The photon and K_L^0 selection cuts are applied except for the variable shown in the plot. The black point shows the data, and the fill histogram shows the Monte Carlo simulation. The red arrow indicates the cut-off value of the variable.	34
5.3	Distribution of the K_L^0 selection variables for the $K_L^0 \rightarrow 3\pi^0$ decay. The photon and K_L^0 selection cuts are applied except for the variable shown in the plot. The black point shows the data, and the fill histogram shows the Monte Carlo simulation. The red arrow indicates the cut-off value of the variable.	35
5.4	Distribution of isolated crystal hit energy(E) vs. its distance(D) from the nearest cluster. The red line shows the cut based on Equation 5.2. The sample was obtained from the $K_L^0 \rightarrow \pi^0\nu\bar{\nu}$ Monte Carlo simulation.[23] .	38
5.5	Beam profile at the exit of the second collimator via the $K_L^0 \rightarrow 3\pi^0$ decay analysis. All the selection cuts are imposed. Filled histograms are predicted by the Monte Carlo simulation.	39
5.6	Distribution of the kinematic variables for the $K_L^0 \rightarrow 3\pi^0$ decay. All the selections are applied except the variable shown in the plot. The black point shows the data, and the fill histogram shows the Monte Carlo simulation. The red arrow indicates the cut-off value of the variable.	40
5.7	Distribution of the kinematic variables for the $K_L^0 \rightarrow 3\pi^0$ decay. All the selections are applied except the variable shown in the plot. The black point shows the data, and the fill histogram shows the Monte Carlo simulation. The red arrow indicates the cut-off value of the variable.	41
6.1	Distribution of cluster timing after relative timing correction. The dot is from real physics data, and the filled histogram is the MC simulation. The red arrow is the cut-off region.	46
6.2	Distribution of total energy from Monte Carlo simulation. The histogram area is normalized to 1. The red arrow is the cut-off region.	47

6.3	An upstream view of the CsI calorimeter. The red region is the outermost boundary, while the blue region is the innermost boundary.	48
6.4	Distribution of veto timing of CC06.	49
6.5	Temporary plots of FBAR and NCC	51
6.6	The schematic geometry diagram of the mechanism of the upstream decay background.	52
6.7	$E_\gamma - R_{XY}$ distributions of scattered $K_L^0 \rightarrow 2\gamma$ decays with various cut. The red frame indicates the signal region. The red number indicates the background level in each region.	52
6.8	The schematic geometry diagram of the mechanism of the fusion cluster background.	53
6.9	$E_\gamma - R_{XY}$ distributions of various background sources after applying all selection cuts. Left-hand side plots exclude the neutron cuts and the right-hand side plots include it. The red frame indicates the signal region. The red number indicates the background level in each region. (Region A indicates the Signal Region and Region B indicates the Blind Region excluding the signal region.)	54
6.10	Example of the energy and timing shapes of photon cluster from the Monte Carlo simulation and neutron cluster from data. The color code represents the deposited energy in MeV and the timing in nanoseconds for each crystal in the cluster. [24]	55
6.11	The architecture of CSD neural network training process.	56
6.12	The ROC curve of the training model. The x-axis is the photon acceptance, and the y-axis is the neutron rejection.	56
6.13	Average pulse shape of the neutron sample (blue dots) and photon sample (red dots) from one CsI crystal.[24]	57
6.14	Distribution of the likelihood ratio for hadronic cluster events (red) and photon cluster events (blue). The photon cluster events are obtained through the $K_L^0 \rightarrow 3\pi^0$ decay analysis of data. The neutron sample is obtained from neutron data.	57
6.15	Illustration of shower depth means. An MPPC is installed on the upstream side. The time difference between the photon arriving upstream and downstream ($\Delta T = T_{MPPC} - T_{PMT}$) is used to measure the depth of the reaction and distinguish between photon events (up) and neutron events (down).	58
6.16	Distribution of the ΔT for neutron events and photon events. The photon cluster events are obtained through the $K_L^0 \rightarrow 3\pi^0$ decay analysis of data. The neutron sample is obtained by scattering neutrons in the beam with an Al plate.	59
6.17	The R_{XY} distribution of the region 2. The red line and arrow indicated the cutoff region	60

6.18 E_γ - H_{XY} distribution of physics data after applying all the selection cuts. The black box is the blind region the red frame is the signal region. The black (red) number is the observed (expected) number of events.	62
6.19 E_γ - H_{XY} distribution of physics data after open the blind box. The black (red) number is the observed (expected) number of events.	62
7.1 Upper limit (left) and signal acceptance (right) for each mass dark photon from 0 MeV to 250 MeV	65

List of Tables

1.1	Theoretical predictions for the branching fractions of the Kaon decays involving massless dark photons. [3]	2
1.2	Main K_L^0 decay background modes and their branching ratios.	3
5.1	Branching ratio of K_L decays	31
5.2	Summary of the veto cut	37
6.1	Main K_L^0 decay background modes and their branching ratios.	45
6.2	Summary of Systematic Uncertainty for SES	59
6.3	Number of events predicted for each source inside the signal region	61

¹ Chapter 1

² Introduction

³ 1.1 Dark Matter and Dark Photons

⁴ Dark matter (DM) is posited to constitute approximately 26.4% of the universe's critical
⁵ density, according to cosmological observations [1]. At this moment the fundamental na-
⁶ ture of dark matter remains one of the most profound mysteries in physics. The Standard
⁷ Model (SM) of particle physics provides no viable explanation for dark matter, prompt-
⁸ ing the motivation to explore physics beyond the Standard Model (BSM). Recent years
⁹ have seen a surge in research aimed at probing the dark sector, with numerous astrophys-
¹⁰ ical and high-energy physics (HEP) experiments making intensified efforts to explore the
¹¹ dark matter.

¹² The dark photon is one of the most promising candidates in the dark sector, it is a new
¹³ type of gauge boson. Theoretically, there are two kinds of dark photons, the massive dark
¹⁴ photon and the massless dark photon. The massive dark photon (A') could mix coupling
¹⁵ with visible photons, to interact with the ordinary particles [1], which means the massive
¹⁶ dark photon is possible to be detected in the experiments. Consequently, the massive
¹⁷ dark photon gets most of the attention in the experimental search for dark photons [2].
¹⁸ However, the massive dark photon has been searched by several experiments, and no
¹⁹ evidence has been observed so far, the parameter space for the massive dark photon
²⁰ has been increasingly constrained. Therefore, our investigation shifts focus towards the
²¹ search for the massless dark photon.

²² The massless dark photon, denoted as $\bar{\gamma}$ in this thesis, is different from the massive
²³ dark photon, it will not directly couple with the Standard Model(SM) particles, and only
²⁴ interact with the SM particles by coupling to the quark. [2] Therefore the massless dark
²⁵ photon is more challenging to be searched in the experiments because it is undetectable.

²⁶ 1.2 Theoretical Predictions

²⁷ There are some theoretical calculations predict that the existence of massless dark pho-
²⁸ tons in the Kaon decay [3]. Assuming the flavor-changing neutral current (FCNC) cou-
²⁹ pling to the d and s quarks, the Kaon meson can decay with missing energy by a massless
³⁰ dark photon. The theories consider the neutral Kaon decay and the charge Kaon channels
³¹ shown in the below Table 1.1.

TABLE 1.1: Theoretical predictions for the branching fractions of the Kaon decays involving massless dark photons. [3]

Decay Channel	Branching Fraction
$K_L \rightarrow \gamma\bar{\gamma}$	$< 1.2 \times 10^{-3}$
$K_S \rightarrow \gamma\bar{\gamma}$	$< 2.1 \times 10^{-6}$
$K_L \rightarrow \pi^0\gamma\bar{\gamma}$	$< 1.0 \times 10^{-6}$
$K_S \rightarrow \pi^0\gamma\bar{\gamma}$	$< 1.8 \times 10^{-9}$
$K_L \rightarrow \pi^+\pi^-\bar{\gamma}$	$< 9.8 \times 10^{-6}$
$K_S \rightarrow \pi^+\pi^-\bar{\gamma}$	$< 1.7 \times 10^{-8}$
$K^+ \rightarrow \pi^+\gamma\bar{\gamma}$	$< 5.6 \times 10^{-7}$
$K^+ \rightarrow \pi^+\pi^0\bar{\gamma}$	$< 2.4 \times 10^{-6}$

Some decay channels in K_L^0 decay can potentially be searched in the KOTO experiment. KOTO Experiment is a rare kaon decay experiment, it is designed to search for the $K_L^0 \rightarrow \pi^0\nu\bar{\nu}$ decay, which is a rare long-lived neutral kaon decay that can provide valuable insights into the CP violation in the Standard Model. $K_L^0 \rightarrow \pi^0\nu\bar{\nu}$ decay has neutrinos in the final state, which become missing energy in the detector because it is undetectable. To probe the missing energy of the neutrino pair, a hermetic veto system was designed to enclose the kaon decay volume. This design can avoid the energy missing from the detectable particle as much as possible, which is beneficial to the search for the missing energy decay channel.

1.3 Basic Strategy of the $K_L^0 \rightarrow \gamma\bar{\gamma}$ Search

From the theoretical perspective shown above, the massless dark photon can be produced in the $K_L^0 \rightarrow \gamma\bar{\gamma}$ decay with the branching fraction of this model up to 10^{-3} . This is well within the sensitivity of the KOTO experiment and is the search Objective of this thesis.

In the $K_L^0 \rightarrow \gamma\bar{\gamma}$ decay, the final state is a photon and a massless dark photon, the photon is detectable in the detector, and the massless dark photon is undetectable.

1.3.1 Signal Identification

$K_L^0 \rightarrow \gamma\bar{\gamma}$ decay requires only one photon cluster to hit the CsI calorimeter and without any in-time hit in the rest of the detector. A single cluster can only provide the energy and position information. The lack of kinematic constraints will be the challenge of this study. Moreover, single cluster signatures are easily mimicked by some unknown background. Requiring a high photon energy may help to suppress this kind of background but also reduce the signal efficiency.

1.3.2 Major Background Sources

The major background sources are K_L^0 decay background and neutron-like background.

⁵⁶ **K_L^0 decay background**

⁵⁷ Table 6.1 shows the main K_L^0 decay backgrounds. Other decay channels are unnecessary to be considered because of the low branching ratio. Only $K_L^0 \rightarrow \pi^\pm e^\mp \nu_e$ and $K_L^0 \rightarrow \pi^\pm \mu^\mp \nu_\mu$ are considered for the decay channel of charged particles in the final state, due to the high branching ratio. To suppress the K_L^0 decay background, studying these decay channels and understanding their characteristics are important. All of these decay channels produce more than one photon in the final state. Therefore, it is easy to suppress these decay channels with the KOTO detector. Except for the decay of $K_L^0 \rightarrow 2\gamma$, whose final state is similar to the signal signature and may be a potentially non-eliminable source of background.

TABLE 1.2: Main K_L^0 decay background modes and their branching ratios.

Decay mode	Branching Ratio
$K_L \rightarrow \pi^\pm e^\mp \nu_e$	$(40.55 \pm 0.11)\%$
$K_L \rightarrow \pi^\pm \mu^\mp \nu_\mu$	$(27.04 \pm 0.07)\%$
$K_L \rightarrow 3\pi^0$	$(19.52 \pm 0.12)\%$
$K_L \rightarrow \pi^+ \pi^- \pi^0$	$(12.54 \pm 0.05)\%$
$K_L \rightarrow 2\pi^0$	$(8.64 \pm 0.06) \times 10^{-4}$
$K_L \rightarrow 2\gamma$	$(5.47 \pm 0.04) \times 10^{-4}$

⁶⁶ **Neutron-like background**

⁶⁷ The neutron originating from the beamline poses a significant background challenge. Accurately simulating the in-beam neutron background is nearly impossible, especially without a defined mechanism to avoid it. The primary method to mitigate this background involves distinguishing the cluster from the photon event.

⁷¹ **1.4 Thesis Overview**

⁷² This thesis presents a detailed study of the $K_L^0 \rightarrow \gamma\bar{\gamma}$ decay in the KOTO experiment. We begin with an overview of the KOTO experiment, describing its detector components and data acquisition (DAQ) system. The analysis section follows, where we elucidate the event reconstruction methods and Monte Carlo simulation techniques employed in the KOTO experiment. Special attention is given to the unique approaches developed for this particular analysis. Subsequently, we delve into the crucial process of Kaon yield estimation and provide an in-depth exploration of the $K_L^0 \rightarrow \gamma\bar{\gamma}$ analysis. This includes background estimation and systematic uncertainty evaluation. In conclusion, we summarize our findings and discuss their implications. The thesis culminates with an outlook on the prospects of the $K_L^0 \rightarrow \gamma\bar{\gamma}$ search within the KOTO experiment, considering potential improvements and challenges.

⁸³ **Chapter 2**

⁸⁴ **KOTO Experiment**

⁸⁵ The KOTO Experiment is a rare decay experiment. The main goal of this experiment is
⁸⁶ to search for the $K_L \rightarrow \pi^0 \nu \bar{\nu}$ decay. The branching ratio of this decay is predicted to be
⁸⁷ $(3.00 \pm 0.30) \times 10^{-11}$ by the Standard Model (SM) [4]. The branching ratio of this decay
⁸⁸ is sensitive to the new physics beyond the SM because of the accuracy. Therefore, the
⁸⁹ KOTO experiment is a good place to search for new physics.

⁹⁰ This chapter will introduce the KOTO detector, outlining the sequence from proton
⁹¹ generation through to data capture within the detector.

⁹² **2.1 J-PARC and Proton Beamlne**

⁹³ The KOTO experiment is located at the Japan Proton Accelerator Research Complex (J-
⁹⁴ PARC)[5] Hadron Experimental Facility (HEF) in Tokai, Japan. Figure 2.1 shows the flow
⁹⁵ of proton beam acceleration, HEF (Hadron Beam Facility) is one of the delivered exper-
⁹⁶ iment facilities. The proton beam has been generated at the end of the linear particle
⁹⁷ accelerator (LINAC)[6], then into a 3 GeV rapid cycling synchrotron (RCS)[7], and finally
⁹⁸ into the main ring synchrotron (MR) to accelerate to 30 GeV[8]. At the end extracted from
⁹⁹ the synchrotron and directed to the HEF, as shown in Figure 2.2.

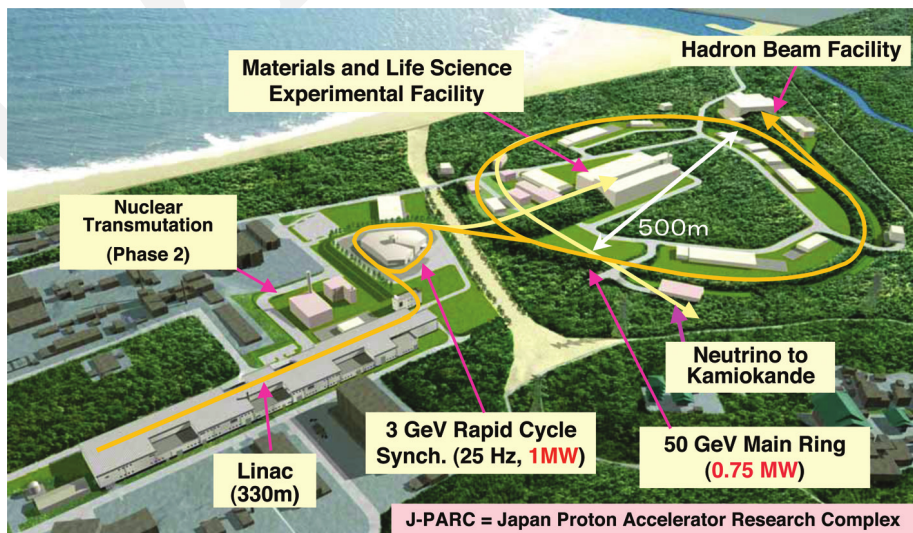


FIGURE 2.1: The entire view of J-PARC. [5]

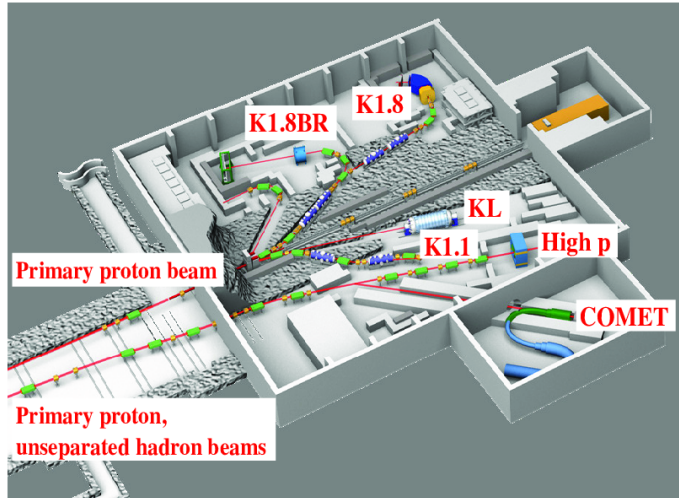


FIGURE 2.2: Illustration of the Hadron Experimental Facility (HEF) at J-PARC.[9] The KL in the Figure indicated the KOTO detector

100 To reduce the instantaneous rate of particles coming into detectors to prevent the event
 101 pileup, a slow-extraction (SX) technique is used. The proton beam was extracted for 2
 102 seconds as a "spill" every 4.22 seconds in 2024 for the beam power of 82 kW. The beam
 103 power is calculated by

$$\text{Beam Power} = E_{\text{proton}} F_{\text{proton}}, \quad (2.1)$$

$$F_{\text{proton}} = N_{\text{spill}}^{\text{proton}} / s_{\text{spill}} \quad (2.2)$$

104 where E_{proton} is the extracted energy of the proton beam, F_{proton} is the protons flux,
 105 $N_{\text{spill}}^{\text{proton}}$ is the number of protons per spill, and s_{spill} is the spill duration.

106 In HEF, the extracted proton beam collides with the T1 target to produce secondary
 107 particles. As shown in Figure 2.3, the T1 target consists of two 66 mm long gold bars with
 108 dimensions of 15×11 mm in cross-section. One bar is used for production and the other
 109 one is a spare. The secondary particles are then directed to the KOTO detector at a 16° to
 110 the beamline.

111 2.2 K_L^0 Beamline

112 After the p-gold collides, a 16° to the beamline was chosen to direct the Kaon beamline
 113 for KOTO. Figure 2.4 shows the schematic diagram of the K_L^0 beamline. To reduce the
 114 photon in the beamline, a 7 cm thick lead photon absorber was installed after the T1
 115 target. Two collimators follow that to narrow the beamline and make it pencil-like. A
 116 sweeping magnet with a 1.2 T magnetic field was installed between the two collimators to
 117 reduce the charged particles in the beamline. A rotatable beam plug is placed between the
 118 sweeping magnet and the 2nd collimator, it is made of brass that could stop the beamline
 119 with most particles. The total length of the beamline is 20 m, which is long enough to
 120 allow the short-lived particles, such as the K_s and hyperons, to decay before reaching
 121 the KOTO detector. Figure 4.1 shows the possible remaining particle at the end of the

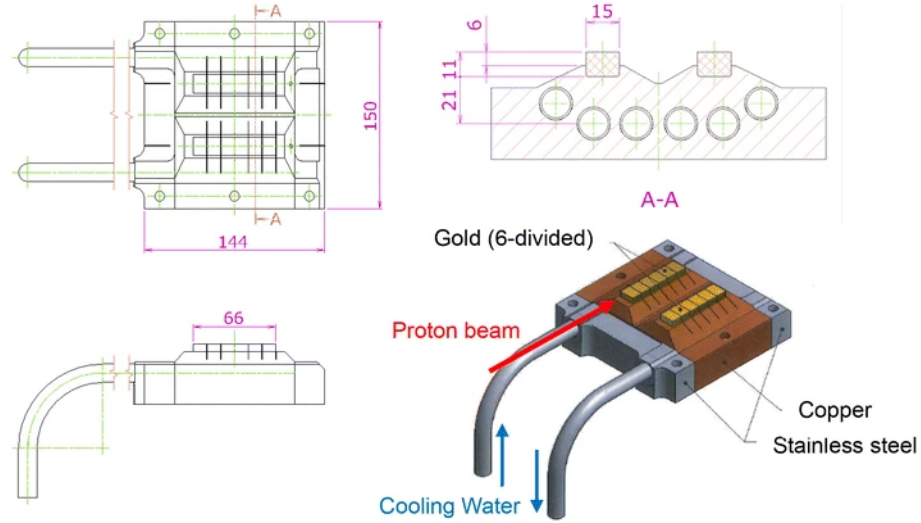


FIGURE 2.3: Structural drawings of the T1 production target [10]. One bar is used for production and the other is a spare.

122 2nd collimator in the beamline which is estimated by the beamline simulation. These
123 particles will enter the KOTO detector.

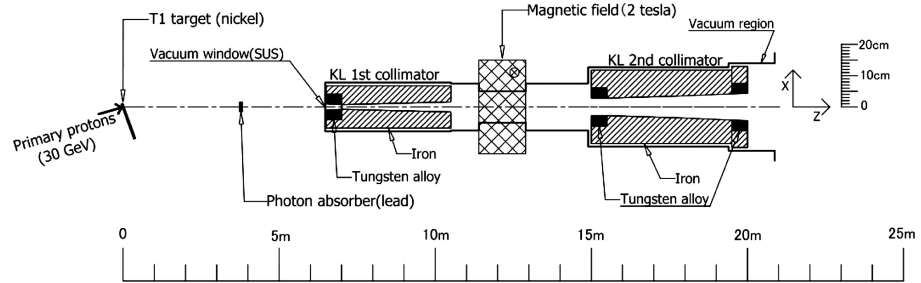


FIGURE 2.4: Schematic diagram of the K_L^0 beamline.[11]

124 2.3 Detectors

125 The KOTO detector is designed to study the decay of K_L^0 particles. Its main components
126 are an electromagnetic calorimeter and a hermetic veto system. As K_L^0 particles enter the
127 detector, they decay within a highly evacuated volume maintained at 5×10^{-5} Pa. The
128 resulting decay products are then detected by various subdetectors. The electromagnetic
129 calorimeter, positioned perpendicular to the beamline, serves primarily as a photon de-
130 tector. Surrounding the decay volume, the hermetic veto system comprises multiple veto
131 counters, including barrel vetoes, charge vetoes, and additional specialized veto coun-
132 ters. This comprehensive veto system ensures efficient detection and differentiation of
133 particle interactions. Figure 2.7 provides a schematic overview of the KOTO detector's
134 layout and components. In this section, the Calorimeter and some important veto coun-
135 ters will be introduced in detail.

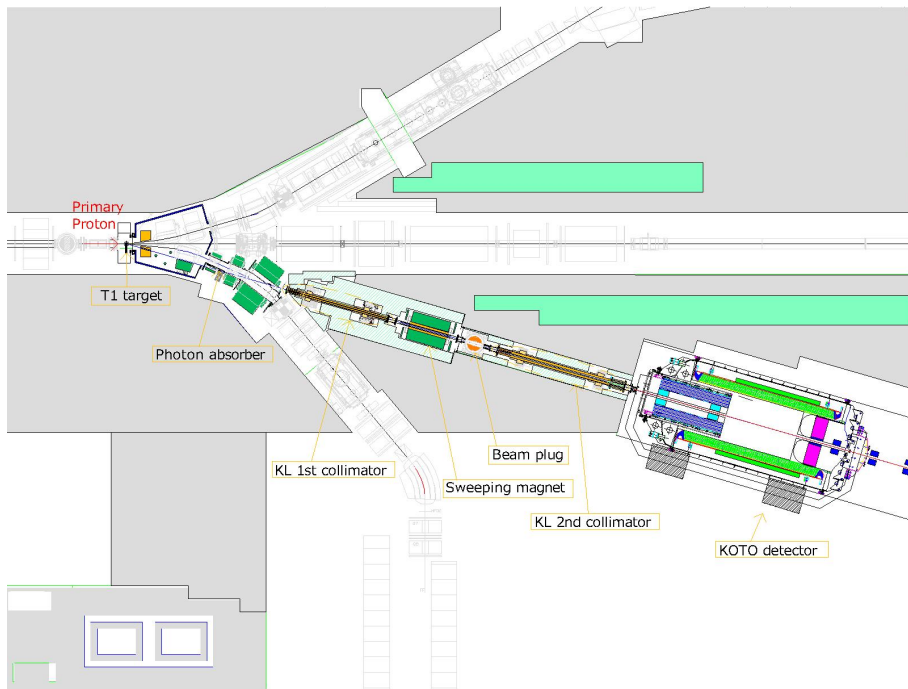


FIGURE 2.5: Beamlne layout

¹³⁶ 2.3.1 CsI

¹³⁷ The electromagnetic calorimeter is the main detector of the KOTO experiment. It is used
¹³⁸ to detect the photon from the K_L decay. The electromagnetic calorimeter consists of 2716
¹³⁹ undoped cesium iodide crystals (CsI). The cross-section of crystals has 2 types of units:
¹⁴⁰ the small crystal is 25×25 mm with 2240 crystals, and the large one is 50×50 mm with
¹⁴¹ 476 crystals. The arrangement of those crystals is shown in Figure 2.6. The depth of the
¹⁴² crystal is 500 mm corresponding to 27 radiation lengths(X_0), in which the X^0 of CsI is
¹⁴³ 18.5 mm. The large crystal depth can contain all the photon energy that can allow us to
¹⁴⁴ ignore the detection inefficiency of the photon. The small crystal size is smaller than the
¹⁴⁵ Molère radius of 35.7 mm, which provides a good resolution of position and the cluster
¹⁴⁶ shape in the x-y plant. That allows us to use the shower shape to distinguish the different
¹⁴⁷ types of clusters on CsI.

¹⁴⁸ A both-end readout system was used in the CsI calorimeter. A photon multiplier tube
¹⁴⁹ (PMT) was connected to the end of each CsI crystal. When a photon hits the CsI, the EM
¹⁵⁰ shower will be induced and the PMT can observe the deposited energy on each crystal.
¹⁵¹ In front of the CsI crystal, 4096 Multi-pixel photon counters (MPPC) were glued. It could
¹⁵² detect the signal of the photon hit from the front end. This readout system can be used to
¹⁵³ measure the shower depth in the calorimeter, by evaluating the time difference between
¹⁵⁴ both ends of the crystal. Which is potentially useful for discriminating the photon cluster
¹⁵⁵ and hadronic-like cluster. Because a hadronic shower is generally deeper than an EM
¹⁵⁶ shower cluster.

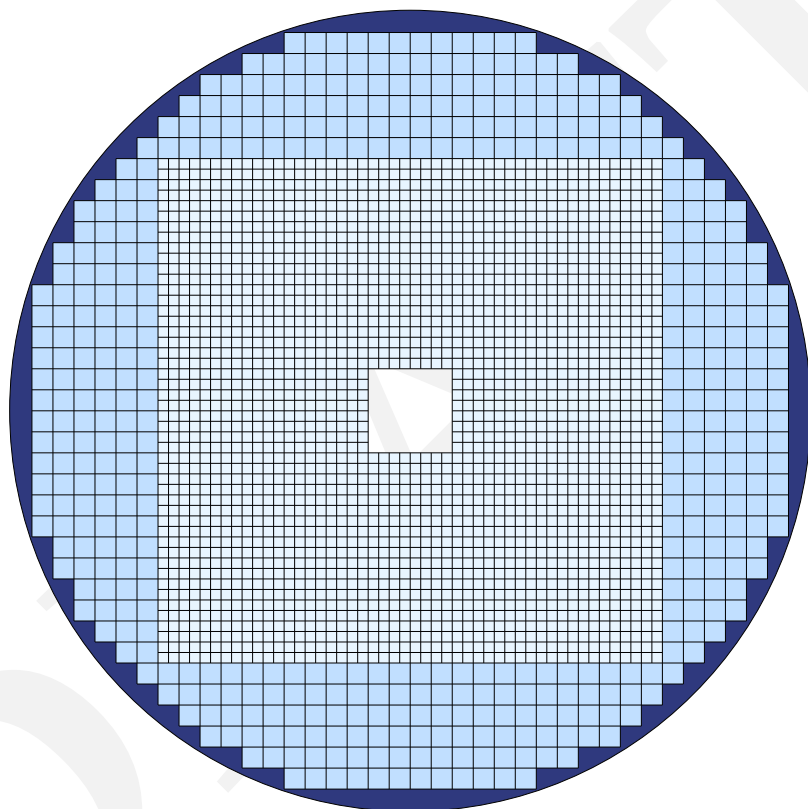


FIGURE 2.6: Schematic diagram of CsI layout.

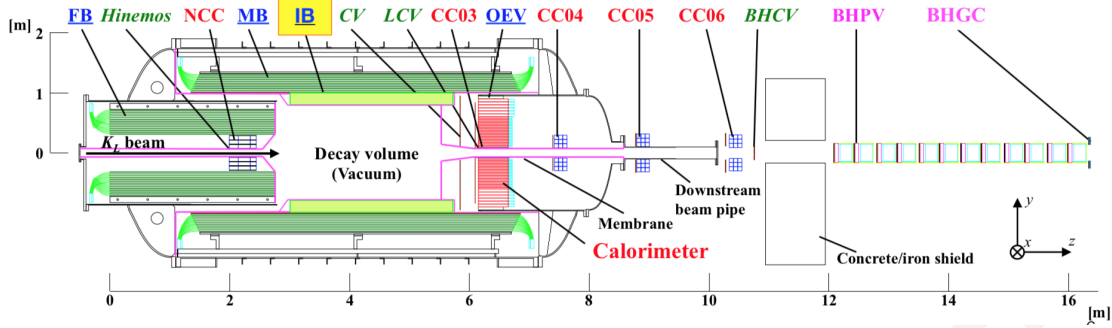


FIGURE 2.7: KOTO detector layout

157 2.3.2 Charge Veto Counter

158 The Charge Veto Counter (CV) is placed in front of the CsI [12, 13, 14]. It is a plant com-
 159 posed of plastic scintillator strips, the arrangement of the strips is shown in Figure 2.8.
 160 Because the CV plant is also perpendicular to the beamline, a square hole was made in
 161 the center of the CV to allow the beamline to pass through. The CV consists of two layers
 162 of 3-mm thick scintillator strips and wavelength-shifting (WLS) fibers, the direction of
 163 the two layers' strips is perpendicular to each other. The front CV is placed 30 cm up-
 164 stream of the CsI, and the Rare CV is placed 5 cm upstream. An MPPC was attached to
 165 both ends of the strip to detect the light emitted by the scintillator.

166 This veto counter was used to detect the charged particle that could hit the CsI calorime-
 167 ter. Because the $K_L^0 \rightarrow \pi^\pm e^\mp \nu_e$ and $K_L^0 \rightarrow \pi^\pm \mu^\mp \nu_\mu$ have a very large branching ratio, the
 168 charged particle could hit the CsI calorimeter and produce a fake photon cluster. The
 169 main purpose of the CV is to veto the charged particle and reduce these two decay chan-
 170 nels. The inefficiency of the CV to a single charge particle is 1.5×10^{-5} .

171 2.3.3 Barrel Veto Counter

172 The Barrel veto counters surround the decay volume which is the main body of the her-
 173 metic veto system to ensure all the photons will not escape from the detector. There are
 174 3 Barrel Veto Counters in the KOTO detector, Front Barrel(FB), Main Barrel(MB), and In-
 175 ner Barrel(IB). The place relation of the three barrel veto counters was shown in Figure
 176 2.9. The MB covered the decay volume, and the IB was placed in the center of the MB,
 177 these two veto counters are used to detect the photon hit escape from the CsI calorime-
 178 ter. The front barrel covers the upstream of the decay region to veto the event decay in
 179 the upstream region. All the barrel veto counters are composed of the lead-scintillator
 180 sandwich structure, as shown in Figure 2.9. The lead was used to absorb the photon and
 181 the scintillator was used to emit the light when the photon hit. After the light emitted by
 182 the scintillator, it will be transferred to the PMT attached to the end of the barrel by WSL
 183 fiber. At the innermost of the MB and IB, a 10 mm thick Charge Veto is attached, which is
 184 called MBCV and IBCV. The MBCV and IBCV consisted of the scintillator and WLS fiber,
 185 which was used to veto the charged particle.

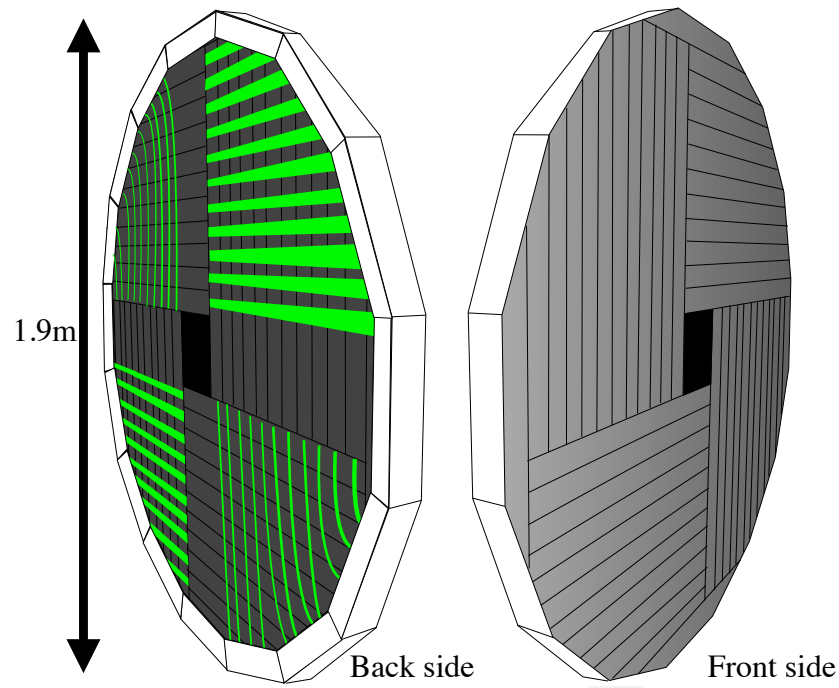


FIGURE 2.8: The Schematic Diagram of Charge Veto Structure.

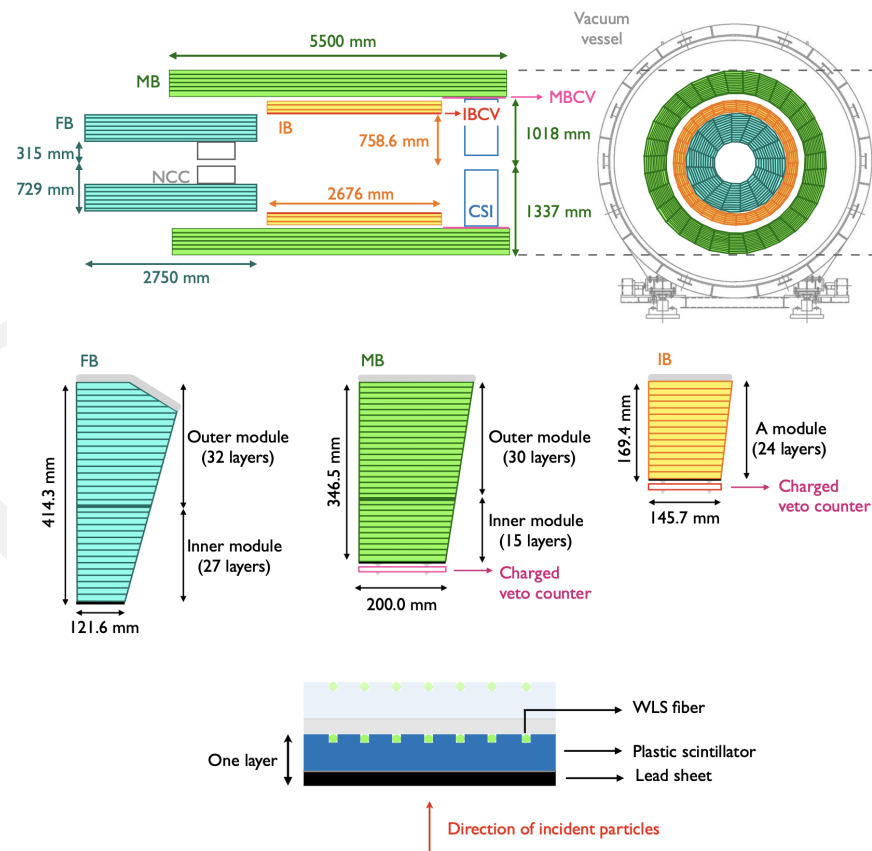


FIGURE 2.9: The Schematic Diagram of Barrel Veto Structure. Figure courtesy of [15].

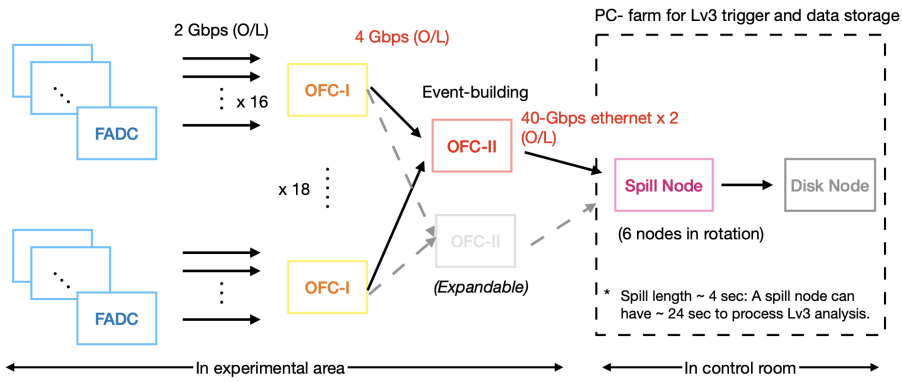


FIGURE 2.10: The architecture of the KOTO DAQ system. [16]

¹⁸⁶ 2.4 Data Acquisition System

¹⁸⁷ When a particle hits the detectors, the electronic signal will be generated. To determine
¹⁸⁸ whether this signal is interesting, a trigger system is used to decide the candidate events.
¹⁸⁹ If an event passes any trigger criteria, the data acquisition system (DAQ) will collect and
¹⁹⁰ store the data.

¹⁹¹ The DAQ system of the KOTO experiment consists of 3 levels: the first-level (L1) and
¹⁹² second-level (L2) trigger placed in the experiment area, and the third-level trigger (L3) at
¹⁹³ the PC farm. The architecture of the DAQ system is shown in Figure 2.10.

¹⁹⁴ KOTO detector has nearly 4000 channels in total, all these channels are connected to
¹⁹⁵ the flash analog-to-digital converter (FADC) board to digitize the signal. There are two
¹⁹⁶ types of FADC boards in the KOTO detector, with 125 MHz and 500 MHz sampling rates.
¹⁹⁷ We have a total of 288 FADC boards and separate them into 18 crates with 16 boards in
¹⁹⁸ each crate.

¹⁹⁹ For the 125 MHz FADC, 16 channels are connected to each board, and the 500 MHz
²⁰⁰ FADC has 4 channels on each board.

201 **Chapter 3**

202 **Event Reconstruction**

203 Event reconstruction is a crucial step in the analysis of decay events. After the reconstruction,
204 the kinematic variable of the K_L^0 , such as the decay vertex, energy, and momentum,
205 can be obtained. With kinematic information, precise event selection can be achieved and
206 the performance of physical analysis can be improved.

207 To reconstruct a K_L^0 decay event, it is necessary to accurately model the decay process.
208 The primary strategy involves initially identifying photon clusters. Subsequently, the
209 clusters' energy, timing, and position on the CsI are utilized to reconstruct the parent
210 particle. This includes determining kinematic properties such as the decay vertex, energy,
211 and momentum of the parent particle. The specific details of the reconstruction process
212 vary depending on the decay mode. For channels involving pions, such as $K_L^0 \rightarrow 3\pi^0$ and
213 $K_L^0 \rightarrow \pi^0\pi^0$, the photon clusters are mapped to pions, which are then used to reconstruct
214 the Kaon. In simpler decay channels like $K_L^0 \rightarrow 2\gamma$, the K_L^0 is directly reconstructed from
215 the photon data.

216 **3.1 Photon Cluster Finding**

217 In this step, we need to find the photon cluster and then reconstruct the energy, timing,
218 and the hit position of the cluster. This process is called "clustering".

219 First, need to find the cluster. The crystal which has deposited energy larger than 3
220 MeV and the hit timing is within 150 ns is considered a "seed crystal". Then, scanning
221 the neighboring crystals in a 140 mm wide square box around the seed crystal. The
222 neighboring crystals will add to the same cluster if the neighboring crystal is also a seed
223 crystal. And do the same scanning process for the neighboring crystals of the neighboring
224 crystals, til there is not a neighboring friend that can be found. This process will be
225 applied to all the seed crystals that have not been assigned to any cluster yet. A seed
226 crystal without any neighboring friend will be defined as an "isolated crystal hit". The
227 isolated crystal hit will be used in the CsI veto. The algorithm is illustrated in Figure 3.1.

228 Because of the wide 150 ns timing window, the cluster may contain the hits not belong
229 to the cluster shower. A seed crystal is assigned to a cluster, but it does not come from
230 the cluster shower will be defined as an "accidental hit" and should be removed from the

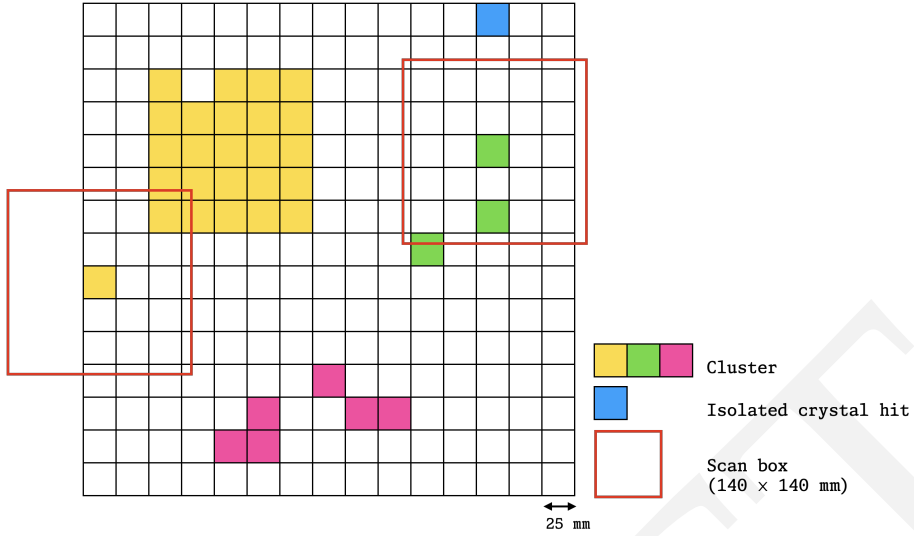


FIGURE 3.1: The illustration of the cluster finding process. All the color crystals are the seed crystals, and the crystals with the same color belong to the same cluster. The black crystal is the isolated crystal hit.

cluster. To avoid the accidental hit, the cluster timing was used to do the selection. The cluster timing ($T_{cluster}$) is defined by the equation 3.1.

$$T_{cluster} = \frac{\sum_{n=1}^{i=1} T_i / \sigma_t^2}{\sum_{n=1}^{i=1} 1 / \sigma_t^2} \quad (3.1)$$

$$\sigma_t = 0.13 \oplus \frac{3.63}{\sqrt{E_i}} \oplus \frac{5}{E_i} \quad (3.2)$$

Where n is the number of crystals in the cluster, i is the i -th crystal, and e is the energy of the cluster. The σ_t is the timing uncertainty of each crystal, which is a function of the energy of each crystal[17]. If a seed crystal from a cluster with timing outside the $\pm 5\sigma$ boundary of its cluster timing, it will be defined as an accidental hit and will be removed. Figure 3.2 shows the timing boundary for a crystal seed after subtracting the cluster timing. The cluster timing will recalculate after removing the accidental hit and iterate this process until all accidental hits have been removed.

Moreover, a timing selection will apply to the clusters. Because the cluster should be produced by the same Kaon decay, the timing of the cluster should be within a certain range. Therefore, the maximum timing difference between all clusters should be within 30 ns. Otherwise, the cluster that has the largest timing difference with the average timing of all clusters will be removed. This process will be repeated until all clusters satisfy the timing selection.

The cluster after the above process will be used in the next step of the reconstruction. The below information on the cluster will be calculated and provided to the next step.

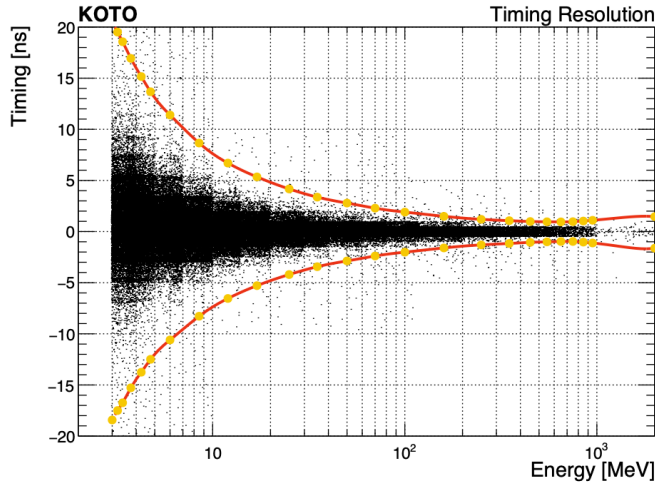


FIGURE 3.2: Timing boundary for a cluster seed based on the scattered plot of crystal timing versus energy deposit. A Gaussian function is fitted at each energy bin and the boundary is defined by $\mu \pm 5\sigma$, where μ and σ are the Gaussian mean and standard deviation. The orange points indicate the boundary at the associated energy bin. The red curve connects all the points for the interpolation of the boundary value between the points. (Figure courtesy of [15])

248 **Cluster Energy ($E_{cluster}$)**

249 The energy of the cluster is the sum of the energy of all crystals in the cluster.

$$E_{cluster} = \sum_{i=1}^n E_i \quad (3.3)$$

250 **Cluster Position ($x_{cluster}, y_{cluster}$)**

251 The position of the cluster is defined by its center of energy, and the position is
252 calculated by the equation below.

$$x_{cluster} = \frac{\sum_{i=1}^n E_i x_i}{E_{cluster}} \quad (3.4)$$

$$y_{cluster} = \frac{\sum_{i=1}^n E_i y_i}{E_{cluster}} \quad (3.5)$$

253 **3.2 Reconstruction of π^0**

254 The π^0 is reconstructed by two photon clusters. Figure 3.3 shows the schematic diagram
255 of the $\pi^0 \rightarrow 2\gamma$ decay process. First, the decay vertex needs to be determined, assum-
256 ing the decay vertex is $(0, 0, z_{vtx})$. Therefore, the three momenta of the photon can be
257 calculated by

$$\vec{P}_\gamma = k \cdot (x, y, \Delta z) \quad (3.6)$$

258 where the k is a constant does not determine yet. And the Δz is the difference between
259 the z position of the cluster and the decay vertex.

$$\Delta z = z_{CsI} - z_{vtx} \quad (3.7)$$

260 Based on four-momentum conservation, the opening angle (θ) between two photons is
261 calculated by

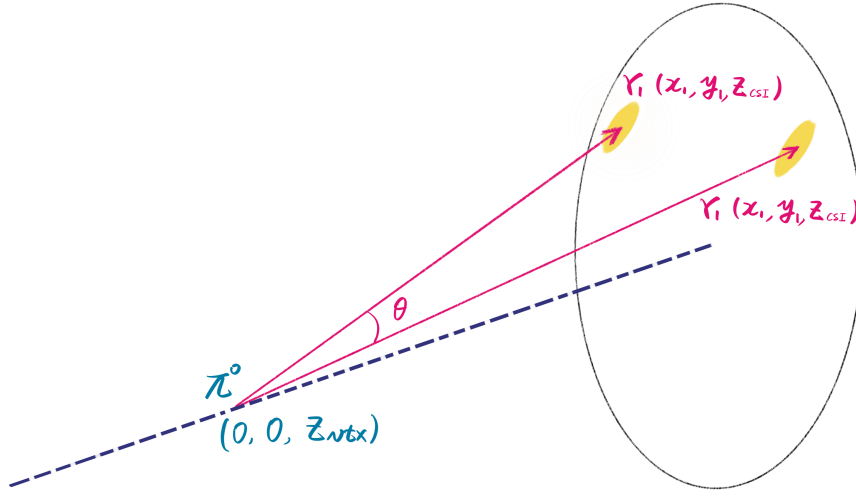


FIGURE 3.3: The schematic diagram of the $\pi^0 \rightarrow 2\gamma$ decay process.

$$\cos(\theta) = 1 - \frac{M_{\pi^0}^2}{2 \cdot E_{\gamma 1} \cdot E_{\gamma 2}} \quad (3.8)$$

and combine with the inner product of two photons' momentum, the following equation can derive the z_{vtx} .

$$1 - \frac{M_{\pi^0}^2}{2 \cdot E_{\gamma 1} \cdot E_{\gamma 2}} = \frac{\vec{P}_{\gamma 1} \cdot \vec{P}_{\gamma 2}}{|\vec{P}_{\gamma 1}| \cdot |\vec{P}_{\gamma 2}|} \quad (3.9)$$

After determining the z_{vtx} , the momentum of the photon can be calculated by

$$|\vec{P}_\gamma| = E_\gamma \quad (3.10)$$

The energy and momentum of the π^0 can be calculated by

$$E_{\pi^0} = E_{\gamma 1} + E_{\gamma 2} \quad (3.11)$$

$$\vec{P}_{\pi^0} = \vec{P}_{\gamma 1} + \vec{P}_{\gamma 2} \quad (3.12)$$

3.3 Reconstruction of Decays

In this section, the reconstruction algorithm for the $K_L^0 \rightarrow 3\pi^0$ and $K_L^0 \rightarrow \gamma\bar{\gamma}$ decay will be introduced. The $K_L^0 \rightarrow 3\pi^0$ decay is used to evaluate the K_L^0 yield, and the $K_L^0 \rightarrow \gamma\bar{\gamma}$ decay is for the physics analysis. In other KOTO experiment studies, the $K_L^0 \rightarrow \pi^0\pi^0$ and $K_L^0 \rightarrow 2\gamma$ decay are also used in the yield estimation and are not covered in this section. Because the $K_L^0 \rightarrow 3\pi^0$ is the only decay channel used for the yield estimation.

All the K_L^0 decay reconstruction is based on the result from the clustering process. A minimal energy selection of 20 MeV is required for the photon cluster. Also, the number of photon cluster requirement need to be equal to the final state of the decay. For the

²⁷⁵ $K_L^0 \rightarrow 3\pi^0$ decay, the event needs to have exactly 6 photon clusters. For the $K_L^0 \rightarrow \gamma\bar{\gamma}$
²⁷⁶ decay, the event should contain only 1 photon cluster.

²⁷⁷ After the K_L^0 decay vertex reconstruction, then calculate the kinematic variables. The
²⁷⁸ kinematic variable will be utilized in the next step analysis.

²⁷⁹ **3.3.1 Reconstruction of $K_L^0 \rightarrow 3\pi^0$**

²⁸⁰ $K_L^0 \rightarrow 3\pi^0$ decay has three π^0 in the decay process, the reconstruction of π^0 will use
²⁸¹ the same algorithm as the previous section. The special situation is there are six photon
²⁸² clusters on the CsI, and the π^0 can be reconstructed in different combinations. All the
²⁸³ combinations will be considered because the true combination is unknown. The most
²⁸⁴ number of combinations for $K_L^0 \rightarrow 3\pi^0$ is

$$\binom{6}{2} \binom{4}{2} \binom{2}{2} / 3! = 15$$

²⁸⁵ Because of the short lift time of the π^0 , the decay vertex of the π^0 's should be very close.
²⁸⁶ Therefore, the χ_z^2 could be used to select the best combination.

$$\chi_z^2 = \sum_i^{N_{\pi^0}} \left(\frac{z_{vtx}^i - \bar{z}_{vtx}}{\sigma_i^2} \right)^2 \quad (3.13)$$

²⁸⁷ where N_{π^0} is the number of π^0 in the decay, z_{vtx}^i is the decay vertex z of the i -th π^0 , \bar{z}_{vtx}
²⁸⁸ is the average decay vertex z of all π^0 , and σ_i is the uncertainty propagated from the
²⁸⁹ calorimeter of the i -th π^0 . The best combination of π^0 should have the smallest χ_z^2 . The
²⁹⁰ weighted average decay vertex z is also defined as the decay vertex z of K_L^0 , calculated
²⁹¹ by

$$\bar{z}_{vtx} = \frac{\sum_i^{N_{\pi^0}} z_{vtx}^i / \sigma_i^2}{\sum_i^{N_{\pi^0}} 1 / \sigma_i^2} \quad (3.14)$$

²⁹² From the π^0 reconstruction, the π^0 decay vertex was assumed in the center of the CsI.
²⁹³ To determine the real decay vertex, a correction process was applied. As shown in Figure
²⁹⁴ 3.4, the K_L^0 travels start from the target and end at the decay vertex, then decay to the π^0 s
²⁹⁵ and γ s hit on the CsI, and K_L^0 project to the center of energy (COE). Therefore, the K_L^0
²⁹⁶ decay vertex can be calculated based on the geometry, by the following equation.

$$x_{vtx} = x_{COE} \cdot \frac{z_{vtx} - z_{target}}{z_{CsI} - z_{target}} \quad (3.15)$$

$$y_{vtx} = y_{COE} \cdot \frac{z_{vtx} - z_{target}}{z_{CsI} - z_{target}} \quad (3.16)$$

²⁹⁷ where z_{target} is the z position of the target. The x_{COE} and y_{COE} can calculate by

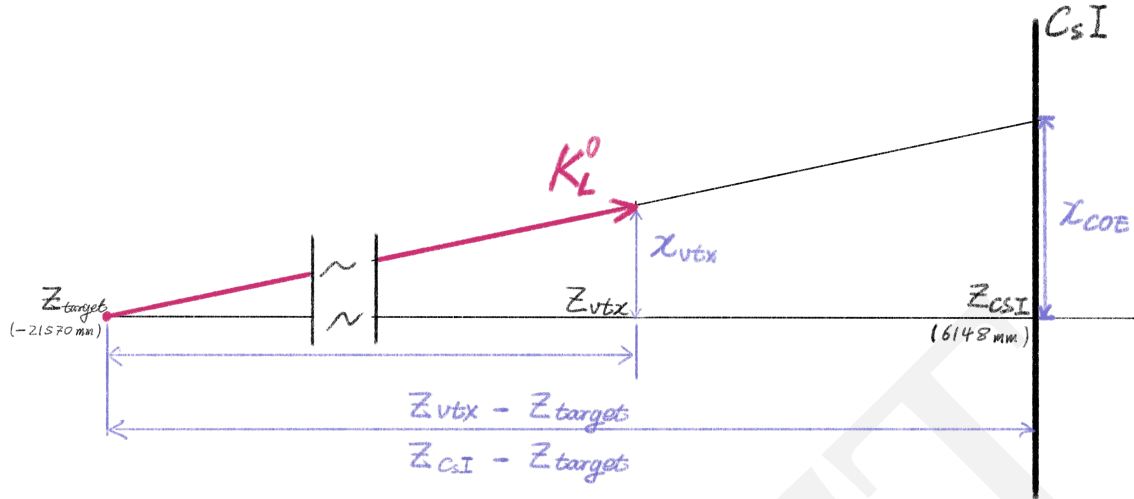


FIGURE 3.4: The schematic diagram of the K_L^0 travel and decay process and geometry relationships

$$x_{\text{COE}} = \frac{\sum_{i=1}^{n_\gamma} E_i x_i}{\sum_{i=1}^{n_\gamma} E_i} \quad (3.17)$$

$$y_{\text{COE}} = \frac{\sum_{i=1}^{n_\gamma} E_i y_i}{\sum_{i=1}^{n_\gamma} E_i} \quad (3.18)$$

After obtaining the corrected decay vertex, the energy and momentum of the K_L^0 can be obtained intuitively from the summation of all the π^0 's energy and momentum, as same as the Equation 3.11.

$$E_{K_L^0} = \sum_{i=1}^{N_{\pi^0}} E_{\pi^0} \quad (3.19)$$

$$\vec{P}_{K_L^0} = \sum_{i=1}^{N_{\pi^0}} \vec{P}_{\pi^0} \quad (3.20)$$

3.3.2 Reconstruction of $K_L^0 \rightarrow \gamma\bar{\gamma}$

$K_L^0 \rightarrow \gamma\bar{\gamma}$ Decay is the primary target of this analysis. The final state of $K_L^0 \rightarrow \gamma\bar{\gamma}$ is similar to $K_L^0 \rightarrow 2\gamma$, but one photon is a dark photon. Due to the missing energy, the signature on CsI of $K_L^0 \rightarrow \gamma\bar{\gamma}$ decay is only one photon cluster hit. Based on Section 3.1, the information that could be obtained from one photon cluster is only its energy, timing, and position on the CsI surface. With this limited information, it is impossible to reconstruct the K_L^0 decay vertex. Therefore, the lack of kinematic information is the biggest challenge of the $K_L^0 \rightarrow \gamma\bar{\gamma}$ decay search study.

3.3.3 Correction for Energy and Position of Photon Clusters

After the reconstruction of the K_L^0 decay, and also obtaining the corrected decay vertex, the energy and position of the photon clusters will be possible to correct. Because this

312 correction process needs the incident angle of the photon, this process has to be done
 313 after the K_L^0 decay reconstruction. After the correction, we will use the new position to
 314 recalculate the decay vertex.

315 **Position Correction**

316 The position of the photon cluster obtained from the clustering process is the position of
 317 the center of energy of the cluster. As shown in the Figure 3.5. The z position for the
 318 center of energy of the cluster is inside the crystal. However, the z position of the CsI
 319 we used in the reconstruction is the position of the crystal surface. This difference will
 320 introduce a bias for the reconstruction of the vertex position. To eliminate this bias, the x
 321 and y positions of the photon cluster need to be corrected to the real incident position.

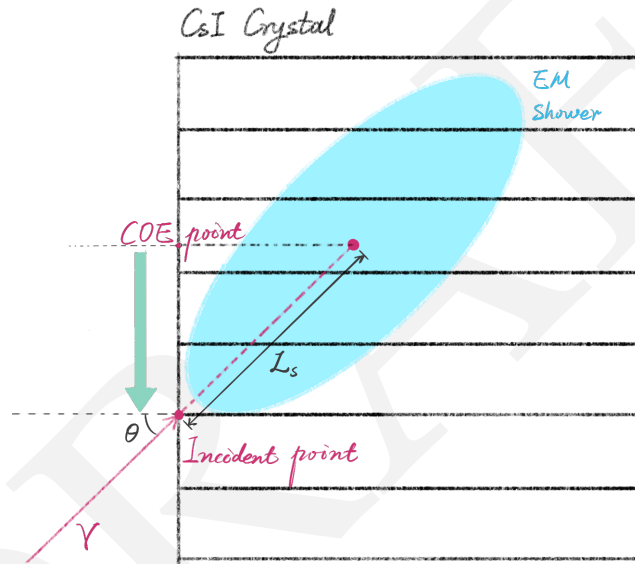


FIGURE 3.5: The schematic diagram of the correction of the photon cluster position.

322 From the decay vertex reconstruction, the incident angle (θ) of the photon was ob-
 323 tained. And the corrected distance (L_c) can be calculated by

$$L_c = L_s \cdot \sin(\theta) \quad (3.21)$$

324 where the L_s is the distance from the incident point to the cluster COE of the EM shower,
 325 and the L_s can be calculated by

$$L_s/X_0 = p_0 + p_1 \ln(E[\text{GeV}]) \quad (3.22)$$

326 where the $X_0 = 18.5$ is the radiation length of the CsI, E is the cluster energy in GeV, and
 327 the $p_0 = 6.490$ and $p_1 = 0.993$ are the parameters obtains from the MC simulation.

328 **Energy Correction**

329 In the clustering process, a 3 MeV energy threshold was applied to the seed crystal. And
 330 EM shower also possibly has leakage energy from the crystals and is not included in the
 331 cluster. These factors will cause the energy lost from the measurement. To correct these
 332 energy losses, a correction function dependence on energy was obtained from the MC
 333 simulation.

$$E_{corr} = E \cdot (1 + w(E)) \quad (3.23)$$

334 where $w(E)$ is the correction function.

335 After the correction of the energy and position of the photon cluster, the decay recon-
 336 struction will be repeated. The final result will be used in the next step of the analysis.

337 **3.4 Veto Hit Reconstruction**

338 The veto counter is used in the background rejection. The rejection is based on the tim-
 339 ing of the veto hit and the deposited energy. And that is the information we need to
 340 reconstruct from the veto hit.

341 The reject criteria require an energy deposit over the energy threshold, which can dis-
 342 tinguish the signal from the background noise, and a hit timing within the timing win-
 343 dow to ensure the hit is from the same K_L^0 decay event, this kind of hit is called an "on-
 344 time" hit. Because the veto information is exclusively utilized for background rejection
 345 criteria in this study, the hit timing was selected as the hit that was closest to the nominal
 346 timing if there was more than one hit on the veto counter.

347 To do the timing criteria, a veto timing(T_{veto}) was defined, which is the difference
 348 between the veto hit timing and the K_L^0 decay timing. The veto timing is defined as

$$\begin{cases} T_{veto} = T_{mod} - T_{vtx} - TOF \\ TOF = D/c, \end{cases} \quad (3.24)$$

349 where the T_{mod} is the veto hit timing, T_{vtx} is the K_L^0 decay timing, TOF is the time-of-
 350 flight of the particle, D is the distance between the decay vertex and the veto hit position.
 351 As shown in the Figure 3.6.

352 However, this equation has to involve the vertex information, which is not available
 353 in the $K_L^0 \rightarrow \gamma\bar{\gamma}$ analysis. Therefore, the T_{veto} needs to be modified to be independent of
 354 the vertex information. The vertex timing T_{vtx} can be approximated by

$$T_{vtx} \approx T_{CsI} - \Delta z/c \quad (3.25)$$

355 where the T_{CsI} is the corrected average timing of the CsI clusters, and the Δz is the
 356 difference between the z position of the CsI surface and the decay vertex. And with the

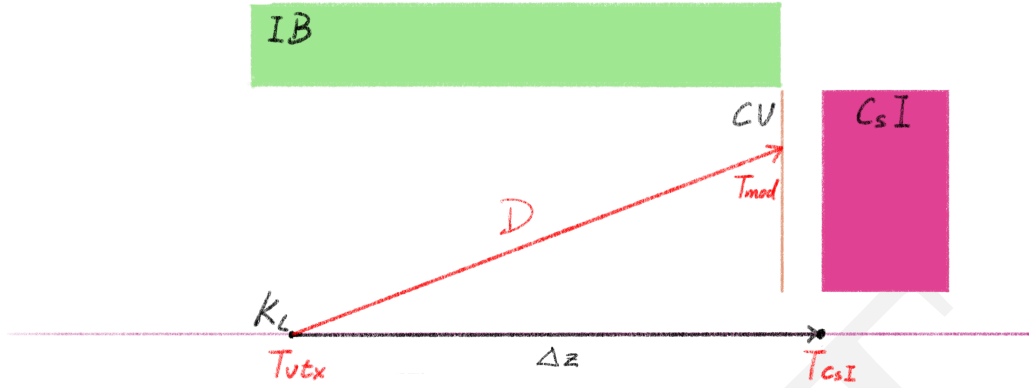


FIGURE 3.6: Schematic view of the timings used in the module-veto-timing calculation.

357 Equation 3.24 the T_{veto} can be derived as

$$T_{veto} \approx T_{mod} - T_{CsI} + (\Delta z - D)/c \quad (3.26)$$

358 The $(\Delta z - D)$ is an uncontrolled variable because D still needs the vertex position information. Thankfully, most veto counters do not have a large scale along the z-axis, thus 359 the variant of the $(\Delta z - D)$ is small. Therefore, $(\Delta z - D)$ can be treated as a constant in 360 most cases, and the T_{veto} can be equivalent to 361

$$T_{veto} \equiv T_{mod} - T_{CsI} \quad (3.27)$$

362 This definition can be used in the all downstream veto count and also the FBAR and the 363 NCC veto counter. However, the Barrel veto counter does not satisfy the condition that 364 has a large scale along the z-axis, and the $(\Delta z - D)$ is not negligible.

365 In the following section, some special treatment of the veto hit will be explained,

366 3.4.1 Barrel Veto Counters

367 The Barrel veto counters contain the Main Barrel(MB) and the Inner Barrel(IB), which 368 have a Both-End Readout system. The mechanism of the both-end readout veto hit is 369 shown in Figure 3.7. And the T_{mod} could be calculated by the upstream and downstream 370 PMT timing.

$$\begin{cases} T_{mod} = T_u - L_u/v, \\ T_{mod} = T_d - L_d/v \end{cases} \quad (3.28)$$

371 where the T_u and T_d are the timing of the upstream and downstream, and $L_u(L_d)$ is the 372 distance between the hit position to the upstream (downstream) PMT, v is the propagated 373 velocity in the module. Therefore, the T_{mod} can be calculated by

$$T_{mod} = \frac{T_u + T_d}{2} - \frac{L}{2v} \quad (3.29)$$

³⁷⁴ The hit position z_{hit} of the veto counter can be derived as

$$z_{hit} = z_{center} + \frac{v \cdot (T_u - T_d)}{2} \quad (3.30)$$

³⁷⁵ where the z_{center} is the z position of the center of the barrel veto counter.

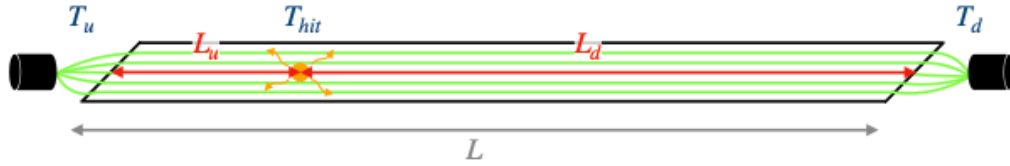


FIGURE 3.7: The Schematic diagram of a photon hit with the generated scintillation lights propagating to both directions and captured by PMTs. Figure courtesy of [15]

³⁷⁶ The geometry relationships of the Barrel veto hit are shown in Figure 3.8. The $(\Delta z - D)$ from Equation 3.26 can be approximated by

$$\Delta z - D \approx \Delta S, \quad (3.31)$$

$$\Delta S = \sqrt{R^2 + (z_{hit} - z_{CsI})^2} \quad (3.32)$$

³⁷⁸ where R is the radius of the Barrel veto counter. And the T_{veto} can be derived as

$$T_{veto} = T_{mod} - T_{CsI} + \Delta S/c \quad (3.33)$$

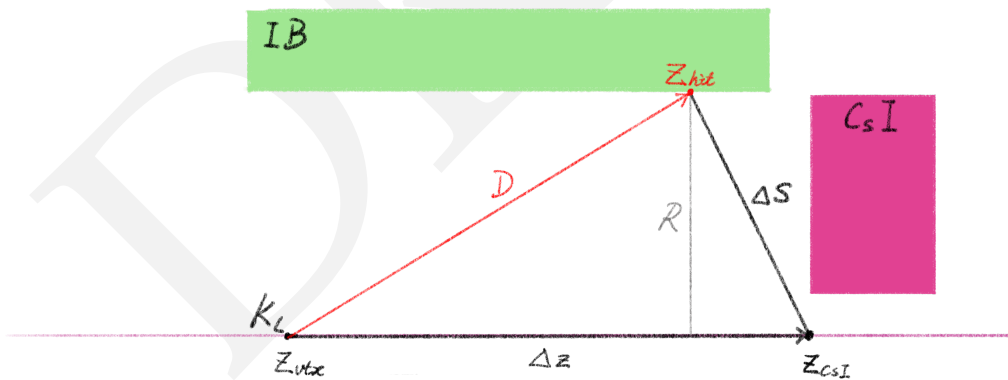


FIGURE 3.8: The Schematic diagram of geometry relationships of the Barrel veto counter.

3.4.2 CsI Calorimeter

³⁸⁰ As Section 3.1 mentioned, the CsI calorimeter is used to reconstruct the photon cluster.
³⁸¹ All the crystal hits on the CsI Calorimeter will be used in the clustering process. How-
³⁸² ever, some crystal hits cannot be assigned to any cluster, and these hits are defined as
³⁸³ "Isolated Crystal Hits". Even though a cluster has been constructed, if it does not satisfy

384 the π^0 reconstruction criteria, it will not be assigned to any K_L^0 or π^0 , and these clusters
 385 are defined as "Extra Clusters". The mechanism of these hits could come from a photo-
 386 nuclear reaction in the shower propagation. These two types of hits will be used in the
 387 veto rejection.

388 Because this detector is also the calorimeter, the veto timing definition needs to be
 389 modified. For the "extra clusters" the timing of the decay vertex (T_{vtx}) is not recalculated
 390 for each cluster,

$$T_{vtx} = T_{cluster} - L/c \quad (3.34)$$

391 where L is the distance between the decay vertex and the cluster.

392 For the "isolated crystal hits", because it possibly split from the other cluster. To avoid
 393 this situation, the selection criteria variables are correlated to the nearest cluster. The
 394 variable that needs to be reconstructed is the distance (D) and the timing difference (T)
 395 between the isolated crystal hit and the nearest cluster.

$$T_{veto} = T_{crystal} - T_{cluster} \quad (3.35)$$

$$D = \sqrt{(x_{crystal} - x_{cluster})^2 + (y_{crystal} - y_{cluster})^2} \quad (3.36)$$

³⁹⁶ **Chapter 4**

³⁹⁷ **Monte Carlo Simulation**

³⁹⁸ In this chapter, the Monte Carlo (MC) simulation of the KOTO experiment is described,
³⁹⁹ which is used for the $K_L^0 \rightarrow \gamma\bar{\gamma}$ analysis. In the HEP analysis field, there are so many
⁴⁰⁰ physics mechanisms behind the physics data, to verify these mechanisms, the MC simu-
⁴⁰¹ lation is used to simulate the physics process to help us understand the data behaviors.
⁴⁰² The simulations were performed to reproduce real physics data and to estimate the K_L^0
⁴⁰³ source background events. The MC simulation should reproduce the real data as much
⁴⁰⁴ as possible. Ideally, if all the background sources and mechanisms are well considered,
⁴⁰⁵ the MC simulation should reproduce the real data perfectly.

⁴⁰⁶ The simulation procedure consists of the following steps. First, generate a set of K_L^0
⁴⁰⁷ particles to enter the KOTO detector, simulate the decay of such particles in the detec-
⁴⁰⁸ tor, and simulate the detector response with the interaction of the decay products. The
⁴⁰⁹ simulation is performed using the GEANT4 toolkit [18, 19, 20]. Then convert the MC sim-
⁴¹⁰ ulation result to the same format as the real data. To reproduce the same conditions of
⁴¹¹ the K_L^0 as the real data run, a K_L^0 momentum spectrum and beam structure are prepared
⁴¹² based on the real data. The MC simulation is performed with the same beam structure
⁴¹³ and detector conditions as the real data. In addition, some other MC simulation is also
⁴¹⁴ performed in this analysis to estimate the background events, such as the beamline sim-
⁴¹⁵ ulation, upstream π^0 background.

⁴¹⁶ **4.1 GEANT4 toolkit**

⁴¹⁷ GEANT4 (GEometry ANd Tracking) is a comprehensive software toolkit, which is pop-
⁴¹⁸ ular in high energy physics, used for the simulation of the passage of particles through
⁴¹⁹ matter. In the GEANT4 simulation, the simulation is performed step by step. In each
⁴²⁰ step, the particle interacts with the detector material, and the energy deposits and the
⁴²¹ direction change of the particle are calculated. The particle quantities are all stored in the
⁴²² simulation output, thus it is easy to analyze the particle decay because its whole proce-
⁴²³ dure is traceable.

424 4.2 Detector Response

425 The GEANT4 simulation toolkit can provide the timing, energy deposit, and position of
 426 the particle interaction, but it is the ideal information, called "true information", which
 427 cannot be directly compared with the real data. The kinematic information is recon-
 428 structed from the data detected by sensors. Therefore, simulations are necessary to repli-
 429 cate the information given by the detector readout.

430 The KOTO detector contains several sub-detectors with different detected principles.
 431 The majority method uses the scintillation process, to detect the propagated light by PMT.
 432 The Čerenkov radiation was used in the BHPV and BHGC, and the gas ionization was
 433 used in the BHCV.

434 4.3 Pulse Simulation

435 The FADC digitized pulses can be described by an asymmetric Gaussian function $f(t)$ as
 436

$$f(t) = A \exp \left(- \left(\frac{t - \mu}{(\sigma_0 + a(t - \mu))} \right)^2 \right) \quad (4.1)$$

437 where t is the time of the pulse, μ is the peak timing, σ_0 and a are the parameters that
 438 determine the shape of the pulse which are given for each detector channel. A is the
 439 normalization factor determined by the integration of $f(t)$ to energy.

440 4.4 K_L^0 Generation

441 In the Monte Carlo simulation, the K_L^0 particles are generated at the K_L^0 beam exit which
 442 is 1507 mm upstream of the detector. Given the momentum and production position of
 443 the K_L^0 particles, the decay process can be simulated. There are two methods that can
 444 obtain the momentum and position distribution, one is called beamline simulation and
 445 the other is called the empirical K_L^0 momentum spectrum.

446 4.4.1 Beamline Simulation

447 The K_L^0 beam in the KOTO experiment is produced from the proton-gold fix target colli-
 448 sions. The simulation that starts from the proton collisions is called the beamline simula-
 449 tion. Because the beamline simulation simulates the whole beamline, the K_L^0 momentum
 450 and position can be obtained directly.

451 In the simulation, a 30 GeV proton beam hit the gold target was simulated. The beam-
 452 line simulation simulates all the structures between the target and the 2nd collimator exit,
 453 such as the photon absorber, sweeping magnet, and two collimators. If any particles re-
 454 main at the 2nd collimator exit, the event will be recorded as an event seed. However,
 455 the beamline simulation is inefficient to generate and cannot reproduce the K_L^0 spectrum

perfectly. In the KOTO experiment, the empirical method is used to obtain the K_L^0 momentum and position distribution.

Although the beamline simulation cannot be used to obtain the K_L^0 spectrum, it is still useful to study the beam contents other than the K_L^0 particles. Figure 4.1 shows the beam content population simulated by the beamline simulation under 10^{12} POT.

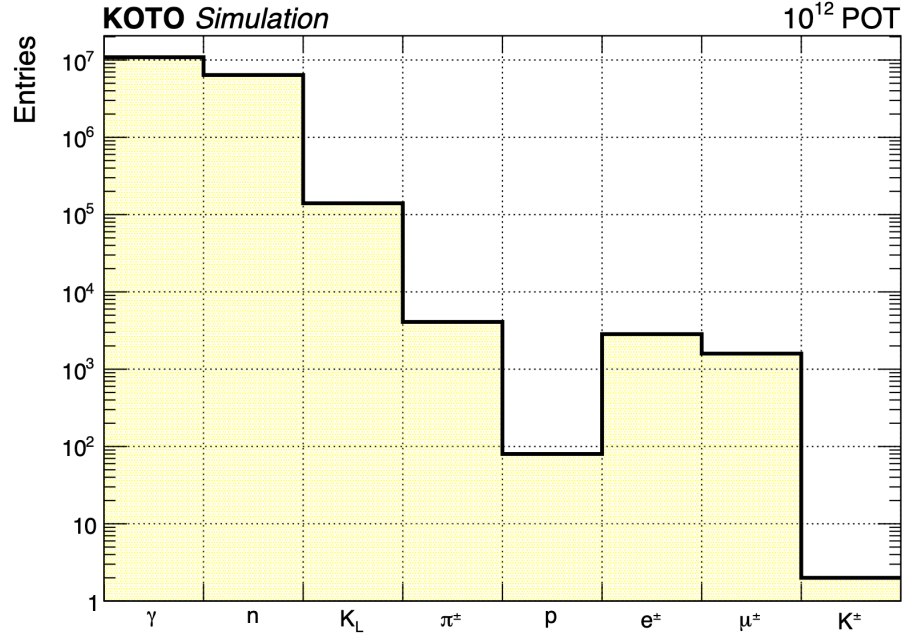


FIGURE 4.1: Beam content at the KOTO detector entrance based on the beamline simulation. Figure courtesy of [15]

In the KOTO experiment, the beamline simulation is used to study some background sources caused by the in-beam particle interaction, such as the NCC background, the halo K_L^0 background, and the Charge Kaon background.

4.4.2 Empirical K_L^0 Spectrum Simulation

The K_L^0 momentum spectrum was obtained from the measurement result of the $K_L^0 \rightarrow \pi^+ \pi^-$ and $K_L^0 \rightarrow \pi^+ \pi^- \pi^0$ decays in 2012 engineering run [21]. Figure 4.2 shows the K_L^0 momentum spectrum which is fitting by the asymmetry Gaussian function as

$$f(p) = \exp\left(-\frac{(p - \mu)^2}{2\sigma_0(1 - (A + Sp)(p - \mu))^2}\right) \quad (4.2)$$

where p is the momentum of the K_L^0 , $\mu = 1.420$ GeV/c is the mean value of the momentum, $\sigma_0 = 0.8102$ GeV/c is the width of the momentum, $A = -0.3014$ and $S = 0.01709$ $(\text{GeV}/c)^{-1}$ are the asymmetry parameters to be determined by fitting.

However, compared to the beamline simulation and empirical model, the K_L^0 particles around the beam core (halo K_L^0 particle) are not reproduced by the empirical model, as

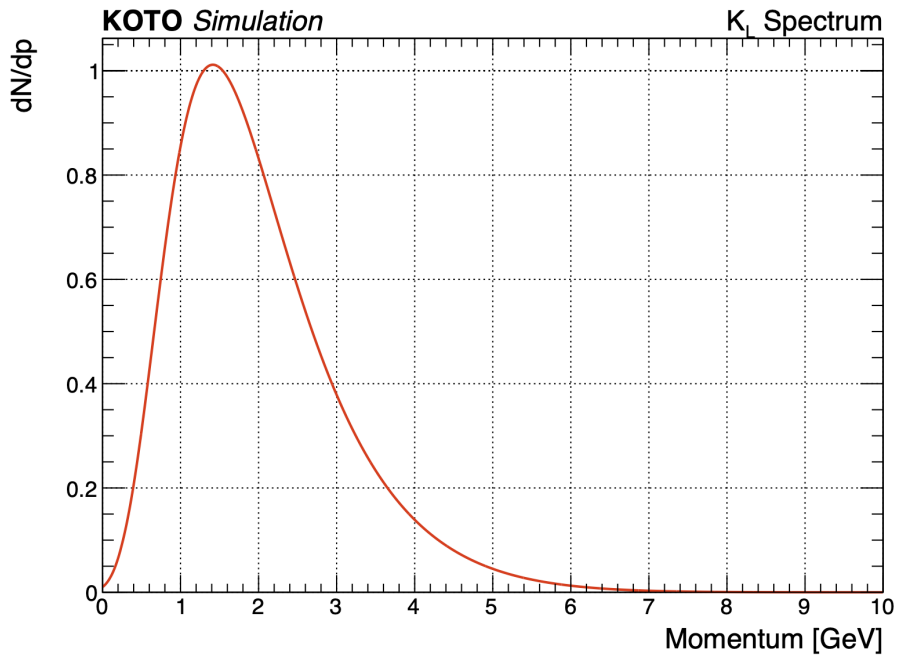


FIGURE 4.2: The K_L^0 momentum spectrum at the exit of the second collimator. Figure courtesy of [15]

473 shown in Figure 4.3. This is because the empirical model does not consider the interactions
 474 in the beamline. Therefore, the halo K_L^0 may contribute to a background source and
 475 need to be emulated by the beamline simulation.

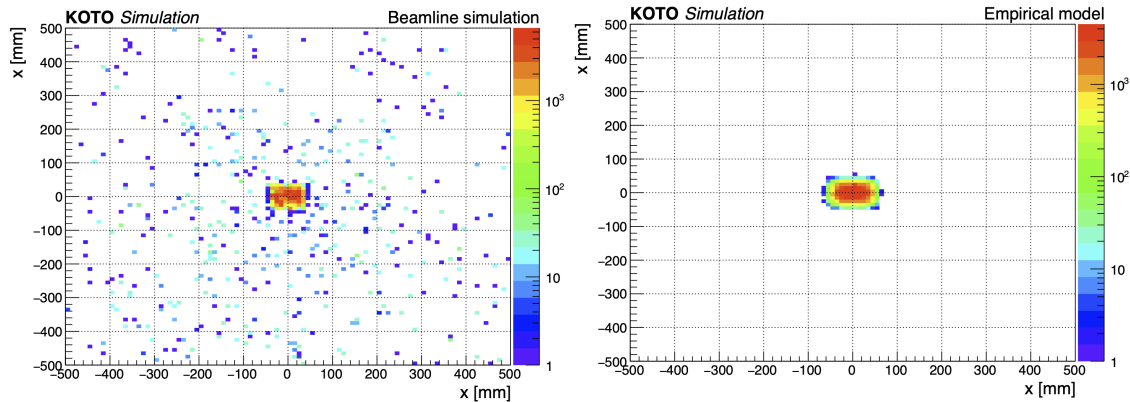


FIGURE 4.3: Comparison of K_L^0 beam profile at the exit of the second collimator between the beamline simulation and the empirical model. Figure courtesy of [15]

476 4.5 Fast Simulation

477 Because the KOTO experiment has a large amount of data, the Monte Carlo simulation is
 478 time-consuming. Especially for the large branching ratio K_L^0 decay channels, such as the
 479 $K_L^0 \rightarrow \pi^\pm e^\mp \nu_e$ and $K_L^0 \rightarrow 3\pi^0$ decays. It not only takes a long time to simulate the decay
 480 process but also occupies a large amount of disk space.

481 Take this study as an example, there are only 2-hour physics data with the protons
 482 on target (POT) of 5.03×10^{16} . A full MC simulation of a $K_L^0 \rightarrow 3\pi^0$ decay would take
 483 approximately 3 days to generate the same decay statistics as data. In this study, we
 484 ended up generating 12 times as many $K_L^0 \rightarrow 3\pi^0$ decays as the same amount of data.
 485 If we use the full MC simulation method, it would take around 30 days to generate the
 486 same statistics. The time consumption does not consider the priority of the batch job
 487 system, which consumes more time in real time. The branching ratio of $K_L^0 \rightarrow \pi^\pm e^\mp \nu_e$
 488 and $K_L^0 \rightarrow \pi^\pm \mu^\mp \nu_\mu$ are even larger than the $K_L^0 \rightarrow 3\pi^0$ decay. To prevent wasting the
 489 whole life being spent on the MC simulation, a fast simulation method is developed to
 490 speed up the MC simulation.

491 The fast simulation method is the same as the full simulation but breaks the generation
 492 process into three steps. In the first step, the K_L^0 and its daughter particles are generated,
 493 and stop the simulation when they hit any detectors. Record the information that we are
 494 interested in. In the second step, make a simple selection of the events to reject the events
 495 that are not interested in. Take the $K_L^0 \rightarrow 3\pi^0$ decay as an example, only the photon
 496 decay from the π^0 was considered. The photon has to hit the CsI fiducial region and the
 497 decay vertex has to be before the CsI. Retention events pass the above selection, require a
 498 minimal number of photons which depends on the study, and require the total energy of
 499 the photon to be larger than the online trigger threshold. In the third step, based on the
 500 information of the retained events, restarted the simulation and simulated the detector
 501 response.

502 The fast simulation method is much faster than the full simulation. In the $K_L^0 \rightarrow 3\pi^0$
 503 decay case, the total MC simulation is done in 10 days which is 3 times faster than the
 504 full simulation. The enhancement of the speed depends on the selection criteria, if a more
 505 strict selection is applied, the enhancement of the speed will be more significant.

506 4.6 Accidental Overlay

507 Because the MC simulation is generated one by one K_L^0 decays which is the ideal simulation
 508 To reproduce the real data situation, the accidental activities need to be considered.
 509 For example, the triggered K_L^0 decay event with another K_L^0 decay coincidently, or the
 510 particle in the beam has some interaction and produces a cluster. To reproduce the acci-
 511 dental activities, the accidental activities were overlaid on the MC simulated events. The
 512 accidental activities' information was taken from the TMON-triggered data, which could
 513 reflect the accidental rate of the real data beam.

514 When doing the accidental overlay, an accidental event is randomly selected from the
 515 library, and superimposed to each channel of the event data. Figure 4.4 shows an example
 516 of an accidental overlay on a simulated pulse for a channel in the FBAR detector.

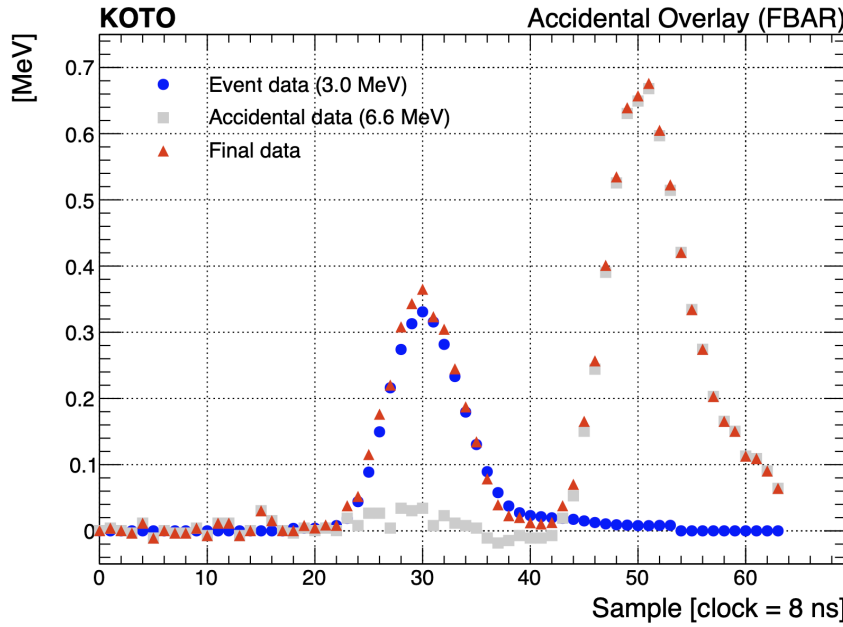


FIGURE 4.4: An example of the accidental overlay on a simulated pulse, subtracting the pedestal.
Figure courtesy of [15]

517 4.7 Neutron background Simulation

518 Neutron background is one of the serious background sources in the KOTO experiment.
 519 As shown in Figure 4.1, there is a large amount of neutron background in the beam.
 520 The mechanism is simply neutron directly interacts with the CsI calorimeter. Because
 521 the GEANT4 toolkit cannot generate a good reliable neutron interaction simulation, a
 522 data-driven method is used to estimate the neutron background. An aluminum plate
 523 target was inserted in front of the KOTO detector entrance perpendicularly to the beam
 524 direction to enhance the neutron in the beam. This target is called the "Z0-Al target" and
 525 the run with the Z0-Al target is called the "Z0-Al run". The Z0-Al run data is used to be
 526 the neutron sample in the background suppression and the estimation study.

⁵²⁷ **Chapter 5**

⁵²⁸ **K_L^0 Yield Estimation**

⁵²⁹ The yield of K_L^0 is an important parameter for most analyses in KOTO. To normalize
⁵³⁰ the Monte Carlo Simulation number of events to the real data, the yield of the K_L^0 was
⁵³¹ required. The K_L yield is usually estimated by well-known neutral decay channels with
⁵³² large branching ratios, which are $K_L^0 \rightarrow 3\pi^0$, $K_L^0 \rightarrow \pi^0\pi^0$, and $K_L^0 \rightarrow 2\gamma$. The branching
⁵³³ ratio of these three decays is shown in the Table 5.1. The background source of these three
⁵³⁴ channels is also limited.

TABLE 5.1: Branching ratio of K_L decays

Decay mode	Branching ratio
$K_L^0 \rightarrow 3\pi^0$	$(19.52 \pm 0.12)\%$
$K_L^0 \rightarrow \pi^0\pi^0$	$(8.64 \pm 0.06) \times 10^{-4}$
$K_L^0 \rightarrow 2\gamma$	$(5.47 \pm 0.04) \times 10^{-4}$

⁵³⁵ The ideal decay channel for the normalization study is $K_L^0 \rightarrow 2\gamma$ decay because the
⁵³⁶ two-photon final state is relatively similar to the $K_L^0 \rightarrow \gamma\bar{\gamma}$ decay. However, due to insuffi-
⁵³⁷ cient time for collecting special run data, the statistics of $K_L^0 \rightarrow \pi^0\pi^0$ and $K_L^0 \rightarrow 2\gamma$ decay
⁵³⁸ are inadequate to estimate the K_L^0 yield. The $K_L^0 \rightarrow 3\pi^0$ decay is a good place to estimate
⁵³⁹ the K_L yield because its branching ratio is far greater than other neutral decay channels,
⁵⁴⁰ and a restrictive requirement of the signal signature. Therefore, the $K_L^0 \rightarrow 3\pi^0$ decay was
⁵⁴¹ accepted to estimate the K_L^0 yield and do the normalization study in this search. If we
⁵⁴² can get more statistics from the data set, we could do On further study of this search with
⁵⁴³ better statistics, the normalization study could be based on $K_L^0 \rightarrow 2\gamma$ decay, and use the
⁵⁴⁴ other two decays to do the cross-check.

⁵⁴⁵ **5.1 Data Set**

⁵⁴⁶ The data set for the normalization study was processed using the entire special run
⁵⁴⁷ physics data, along with the normalization trigger. The pre-scaling factor of 13 means
⁵⁴⁸ that for every 13 events triggered, only one event was stored. For the control sample,
⁵⁴⁹ we employed a Monte Carlo simulation of $K_L^0 \rightarrow 3\pi^0$ decay that includes accidental

550 overlays. Approximately 1×10^9 $K_L^0 \rightarrow 3\pi^0$ decay events were simulated for this con-
 551 trol sample. Due to the distinct 6-cluster event signature characteristic of the $K_L^0 \rightarrow 3\pi^0$
 552 decay, the influence of other decay modes is negligible in the normalization study.

553 5.2 Event Selections

554 In the K_L^0 Yield study, the objective of event selection is to isolate $K_L^0 \rightarrow 3\pi^0$ decay events
 555 while effectively rejecting background events. This selection process comprises two main
 556 components: the veto cut and the kinematic cut. The veto cut is straightforward, requir-
 557 ing an in-time hit in the veto counter. The kinematic cut, on the other hand, utilizes
 558 photon data and the reconstructed physical quantities of K_L^0 and π^0 . This cut is further
 559 divided into three categories: Trigger Cut, Photon Selection, and K_L^0 Selection. A detailed
 560 explanation of these cuts will be provided in the following section.

561 5.2.1 Trigger Cut

562 Due to the inability of the Monte Carlo simulation to accurately replicate the online Data
 563 Acquisition (DAQ) system, it does not impose the same trigger conditions as those found
 564 in the actual data. Consequently, the trigger cut was introduced to eliminate the effects
 565 of the online triggers, thereby enhancing the comparability between simulated and real
 566 data.

567 Trigger Timing Window

568 In one 64-sample window, there may maybe more than one trigger hit. If there are sep-
 569 arate events, it may cause a double counting of overlay events. To eliminate the bias
 570 from this effect, an average photon timing window of ± 15 ns of the nominal timing was
 571 required.

572 Total Energy in CsI

573 The online Total energy in CSI (CSIET) threshold is set as 500 MeV in the special physics
 574 run normalized trigger. To eliminate this online effect, a CSIET threshold offline was
 575 required higher than the online threshold. In this study, an offline CSI_{ET} threshold of
 576 650 MeV was required, which is the same as the $K_L^0 \rightarrow \pi^0\nu\bar{\nu}$ study. The offline CSIET
 577 threshold is determined by examining the ET efficiency curve, as explained in Section
 578 6.3.1 of Jay's dissertation[15].

579 5.2.2 Photon Selection

580 Figure 5.1 shows the distribution of the photon selection variables for the $K_L^0 \rightarrow 3\pi^0$
 581 decay. The photon selection cuts include the photon energy, photon hit position, and
 582 minimum cluster distance. These cuts are based on the photon information and are used
 583 to select photons with good reconstruction reproducibility.

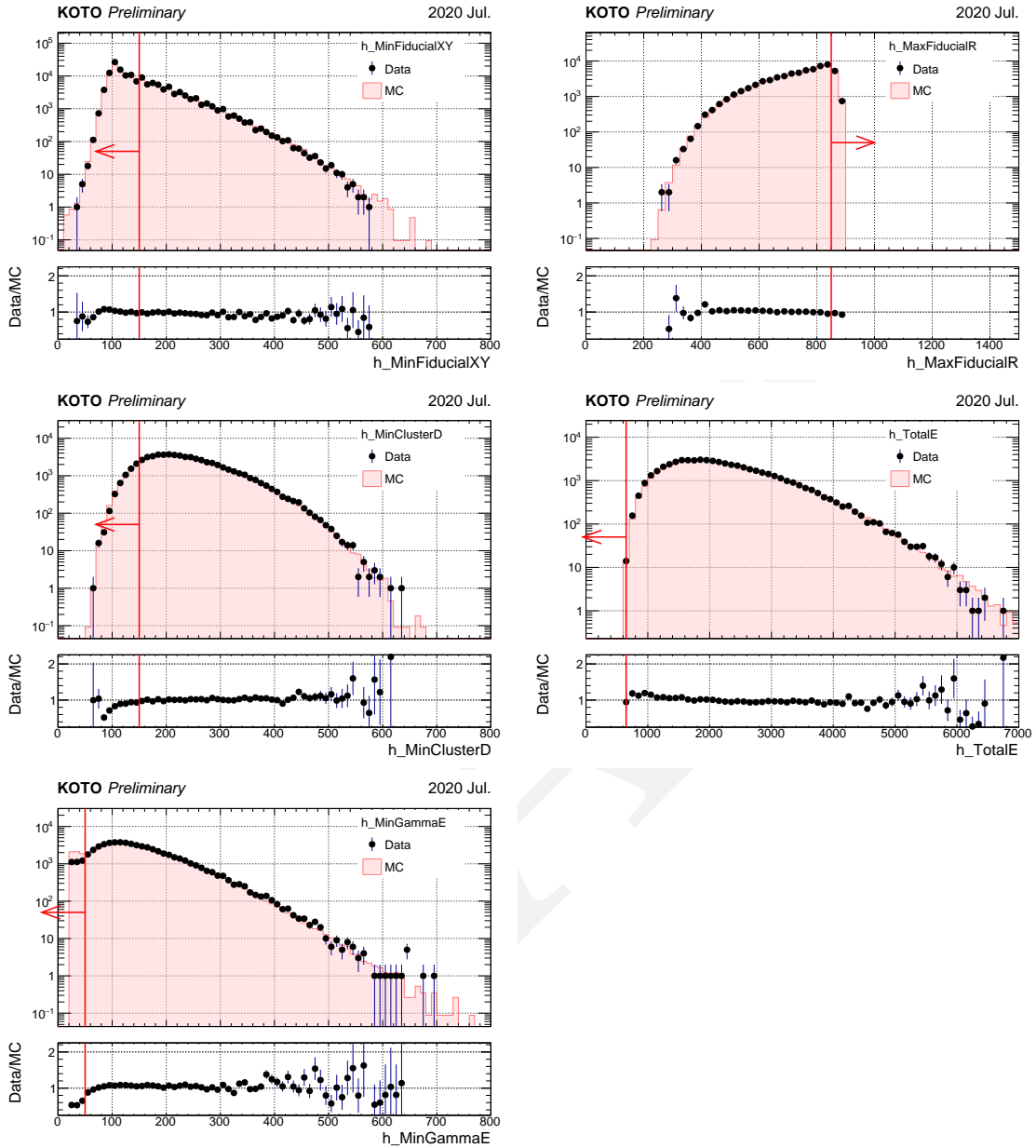


FIGURE 5.1: Distribution of the photon selection variables for the $K_L^0 \rightarrow 3\pi^0$ decay. The photon selection cuts are applied except for the variable shown in the plot. The black point shows the data, and the fill histogram shows the Monte Carlo simulation. The red arrow indicates the cut-off value of the variable.

584 **Photon Energy (E_γ)**

585 To improve the reconstruction quality of the photon, the ultra-soft photon with energy
586 less than 50 MeV was rejected.

587 **Photon Hit Position (Fiducial Cut)**

588 To ensure the EM shower was well contained in the CsI calorimeter, a photon hit position
589 cut was applied. Any photon in an event that hit the outermost and innermost edge

of the CsI calorimeter was rejected. This cut is also called the Fiducial Cut. The outer boundary requires the radius of the photon hit position within 850 mm, $R_\gamma < 850$ mm, while the inner boundary requires the photons 150 mm away from the square beam hold, $\min\{|x_\gamma|, |y_\gamma|\} > 150$ mm.

594 Minimum Cluster Distance

If two-photon clusters are too close to each other, the EM shower may overlap, and the energy reconstruction will be incorrect, or the two photons may be misidentified as one photon. To avoid this situation, a minimum cluster distance of 150 mm was required.

598 5.2.3 K_L^0 Selection

Figure 5.2 and 5.3 show the distribution of the K_L^0 selection variables for the $K_L^0 \rightarrow 3\pi^0$ decay. The K_L^0 selection cuts include the χ^2 of the decay Z, ΔT of the vertex, K_L^0 decay vertex Z, K_L^0 mass, $K_L^0 P_T$, $\Delta\pi^0$ mass, and $K_L^0 \Delta Z_{vtx}$.

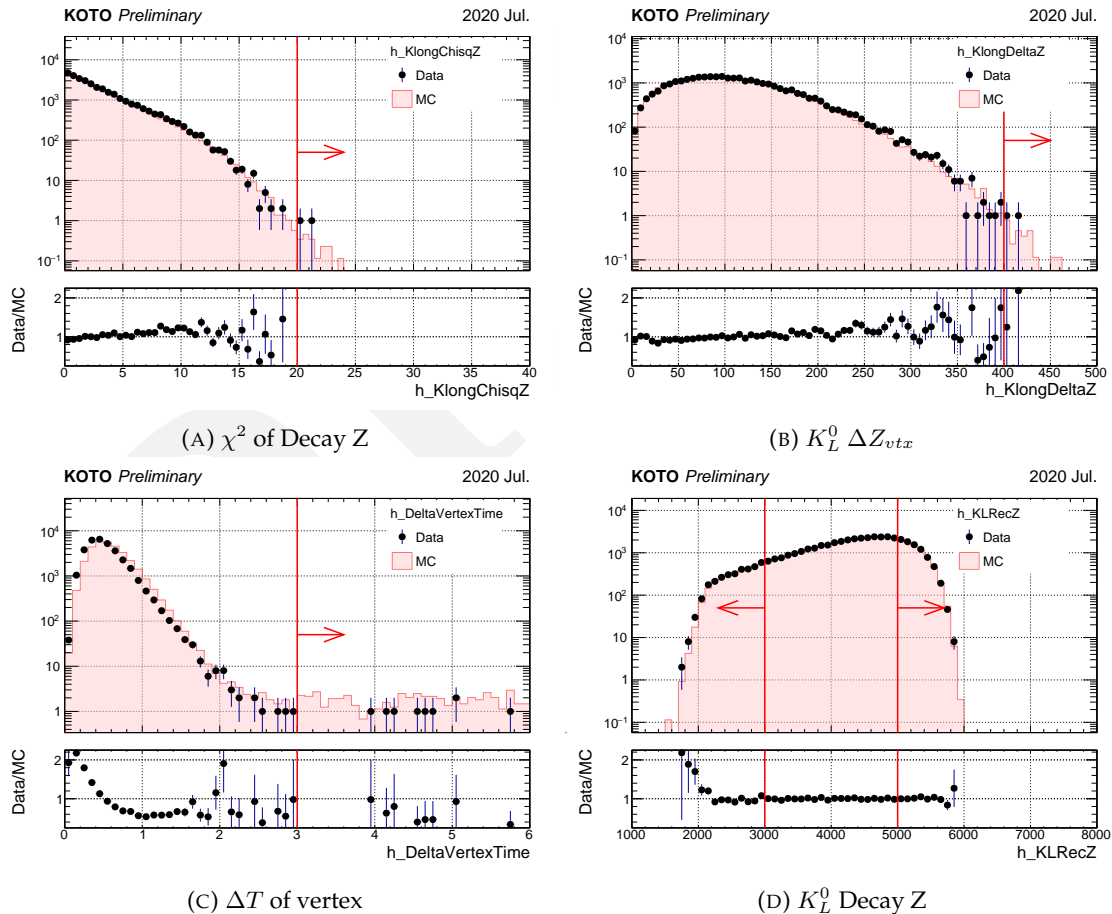


FIGURE 5.2: Distribution of the K_L^0 selection variables for the $K_L^0 \rightarrow 3\pi^0$ decay. The photon and K_L^0 selection cuts are applied except for the variable shown in the plot. The black point shows the data, and the fill histogram shows the Monte Carlo simulation. The red arrow indicates the cut-off value of the variable.

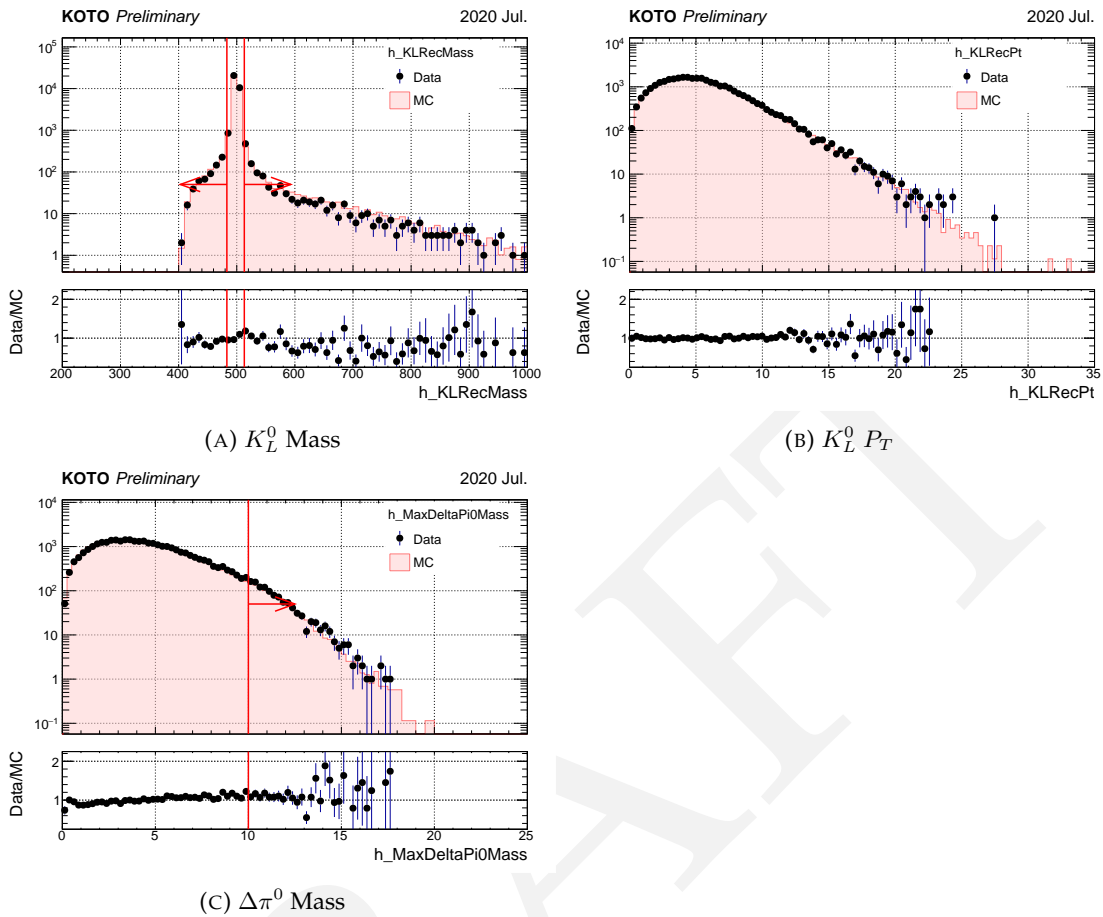


FIGURE 5.3: Distribution of the K_L^0 selection variables for the $K_L^0 \rightarrow 3\pi^0$ decay. The photon and K_L^0 selection cuts are applied except for the variable shown in the plot. The black point shows the data, and the fill histogram shows the Monte Carlo simulation. The red arrow indicates the cut-off value of the variable.

$$\chi^2_z$$

To make sure the reconstructed π^0 is good quality, the χ_z^2 cut was applied. The χ_z^2 could indicate the goodness of the photon pair to the π^0 reconstructed, defined in Equation 3.13. This cut was used to ensure the consistency of the reconstructed π^0 vertex, and the χ_z^2 was required to be less than 20.

$$K_L^0 \Delta Z_{vtx}$$

The ΔZ_{vtx} is defined as the maximum difference between the reconstructed π^0 's, as shown in Equation 5.1. This cut is also used to ensure the consistency of the reconstructed π^0 vertexes. The ΔZ_{vtx} was required to be less than 400 mm.

$$\Delta Z_{vtx} = \max \left(|Z_{vtx}^i - Z_{vtx}^j| \right) \quad (5.1)$$

611 **Maximum Difference of Vertex Timing (ΔT_{vtx})**

612 The vertex timing of each photon cluster that belongs to the same event should be con-
 613 sistent with each other. The maximum vertex timing difference between reconstruction
 614 K_L^0 and each photon cluster was required to be less than 3 ns.

615 **K_L^0 Decay Vertex Z (Z_{vtx})**

616 The Decay vertex of the K_L^0 was required within the decay volume of the KOTO detector,
 617 $3000 \text{ mm} \leq Z_{vtx} \leq 5000 \text{ mm}$.

618 **K_L^0 Mass**

619 In the reconstruction of K_L , the invariant mass of photons was required to be within
 620 $\pm 15 \text{ MeV}/c^2$ of the nominal K_L mass of $497.614 \text{ MeV}/c^2$ [22]. This criterion significantly
 621 reduces event contamination from mispairing in both the $K_L \rightarrow 3\pi^0$ analyses. It also
 622 minimizes the interference of $K_L \rightarrow 3\pi^0$ decays in the analysis.

623 **$K_L^0 P_T$**

624 In the normalization study, K_L^0 should not have missing particles, so the reconstructed
 625 transverse momentum (P_T) of the K_L^0 is expected to be small. The P_T of the K_L^0 was
 626 required to be less than 50 MeV/c.

627 **$\Delta\pi^0$ Mass**

628 The $\Delta\pi^0$ mass is the difference between the reconstructed π^0 mass and the nominal π^0
 629 mass of $134.9766 \text{ MeV}/c^2$ [22]. The π^0 mass was calculated by the reconstructed K_L^0 de-
 630 cay vertex. A large $\Delta\pi^0$ mass indicates a bad pairing of the photon cluster, which may
 631 come from the accidental hit. The reconstructed $\Delta\pi^0$ mass was required to be within
 632 $\pm 10 \text{ MeV}/c^2$ of the nominal π^0 mass.

633 **5.2.4 Veto Cut**

634 All the veto cuts applied to the yield study are the same as the veto cuts used in the
 635 $K_L^0 \rightarrow \pi^0\nu\bar{\nu}$ analysis[15]. The summary of the veto cut is shown in Table 5.2.

636 In the following section, a detailed explanation of the Veto Cut is shown.

637 **Isolated Crystal Veto**

638 An isolated crystal hit very close in time to the photon clusters are possibly comes from
 639 the same K_L^0 decay. To reject this kind of background, a timing window of $\pm 10 \text{ ns}$ of the
 640 nearest photon cluster timing is required in this veto. A multistep cut based on the hit
 641 Energy(E) and Distance(D) from the closest cluster is applied, as the following equation:

TABLE 5.2: Summary of the veto cut

Veto Counter	Energy Threshold	Timing Window
FB	1 MeV	51ns
NCC and HINEMOS	1 MeV	40ns
MB	1 MeV	20ns
IB	1 MeV	20ns
MBCV	0.5 MeV	60ns
IBCV	0.5 MeV	60ns
CV	0.2 MeV	20ns
LCV	0.6 MeV	30ns
CSI (isolated crystal)	see Sec. 5.2.4	20ns
CSI (extra cluster)	see Sec. 5.2.4	20ns
OEV	1 MeV	20ns
CC03	3 MeV	30ns
CC04, CC05, CC06 (CSI crystal)	3 MeV	30ns
CC04, CC05, CC06 (plastic scintillator)	1 MeV	30ns
BPCV	1 MeV	24ns
BHCV ¹	221 eV	25ns
BHPV ²	2.5 p.e.	15ns
BHGC ³	2.5 p.e.	15ns

¹ BHCV requires hits in more than two modules.

² BHPV requires hits in more than three consecutive modules.

³ BHGC veto accepts the number of equivalent photons instead of energy.

$$\begin{cases} E > 10 \text{ [MeV]} & , \text{if } D < 200 \text{ [mm]} \\ E > 10 - \frac{7 \cdot (D-200)}{400} \text{ [MeV]} & , \text{if } 200 \leq D \leq 600 \text{ [mm]} \\ E > 3 \text{ [MeV]} & , \text{if } D > 600 \text{ [mm]} \end{cases} \quad (5.2)$$

642 As shown in Figure 5.4, a higher energy threshold is required for the isolated crystal
 643 to hit nearer to the cluster, to bypass the shower propagation effect.

644 Extra Cluster Veto

645 A cluster hit in the CsI calorimeter that is not associated with the π^0 decay is considered
 646 an extra cluster. If the timing of the extra cluster is within ± 10 ns of the reconstructed π^0
 647 vertex time, it is considered as a background and rejected.

648 5.3 Yield Estimation

649 The Yield of the K_L^0 (Y) in the data set is defined by the following equation:

$$Y = \frac{N_{mode}}{\mathcal{BR}_{mode} \times A_{mode}} \quad (5.3)$$

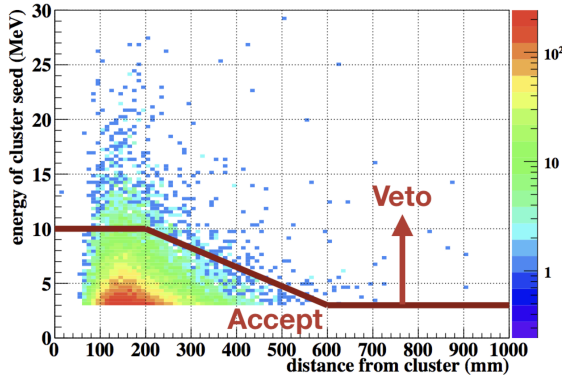


FIGURE 5.4: Distribution of isolated crystal hit energy(E) vs. its distance(D) from the nearest cluster. The red line shows the cut based on Equation 5.2. The sample was obtained from the $K_L^0 \rightarrow \pi^0 \nu \bar{\nu}$ Monte Carlo simulation.[23]

650 where N_{mode} is the number of events, \mathcal{BR}_{mode} is the branching ratio, and A_{mode} is the
 651 acceptance. The mode could be any decay channel of the K_L^0 . The acceptance(A_{mode}) can
 652 be evaluated by the Monte Carlo simulation, as the following equation:

$$A_{mode} = \frac{N_{remaind}}{N_{gen}} \quad (5.4)$$

653 where $N_{remaind}$ is the number of events that pass the event selection, and N_{gen} is the
 654 number of generated K_L^0 decays. And because the K_L^0 yield is proportional to the number
 655 of protons on target (POT), the K_L^0 flux (F) can be defined as the yield per POT, as shown
 656 in the following equation:

$$F = \frac{Y}{POT} \quad (5.5)$$

657 As mentioned in Section 5.1, the normalization trigger was used to be the data sample.
 658 Because the normalization trigger was taken simultaneously with the physics trigger, the
 659 K_L^0 yield is the same as the physics trigger. Therefore, the K_L^0 yield evaluated by the
 660 normalization trigger can be used directly in the physics analysis.

661 In this study, the K_L^0 yield was estimated by the $K_L^0 \rightarrow 3\pi^0$ decay. All the kinematic
 662 cuts introduced in Section 5.2.2 and 5.2.3 and the veto cuts summarized in Table 5.2 were
 663 imposed.

664 5.3.1 Estimation by $K_L^0 \rightarrow 3\pi^0$ Decays

665 Figure 5.6 and 5.7 show the distribution of the kinematic variables for the $K_L^0 \rightarrow 3\pi^0$
 666 decay after imposed all selection cuts referred in Section 5.2. The purity of the $K_L^0 \rightarrow 3\pi^0$
 667 decay is high because there is no other K_L^0 decay mode that can mimic the six-cluster
 668 signature on CSI. The most discrepancy comes from the statistics of the special physics
 669 data is not enough to match the Monte Carlo simulation.

670 Figure 5.5 shows the beam shape of the x and y projection at the exit of the second
 671 collimator. The beam core shows a good agreement between the data and the Monte
 672 Carlo simulation.

673 5.4 Summary of K_L^0 Yield Estimation

674 The K_L^0 yield of the special physics run was estimated to be 1.29×10^{10} by the $K_L^0 \rightarrow 3\pi^0$
 675 decay. The systematic uncertainty will be considered in the Single Event Sensitivity (SES)
 676 study in Section 6.5.1.

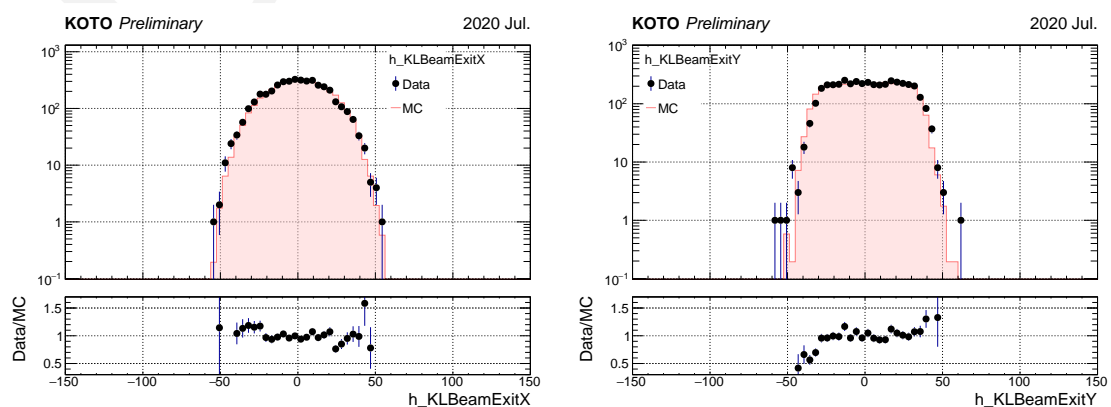


FIGURE 5.5: Beam profile at the exit of the second collimator via the $K_L^0 \rightarrow 3\pi^0$ decay analysis.
 All the selection cuts are imposed. Filled histograms are predicted by the Monte Carlo simulation.

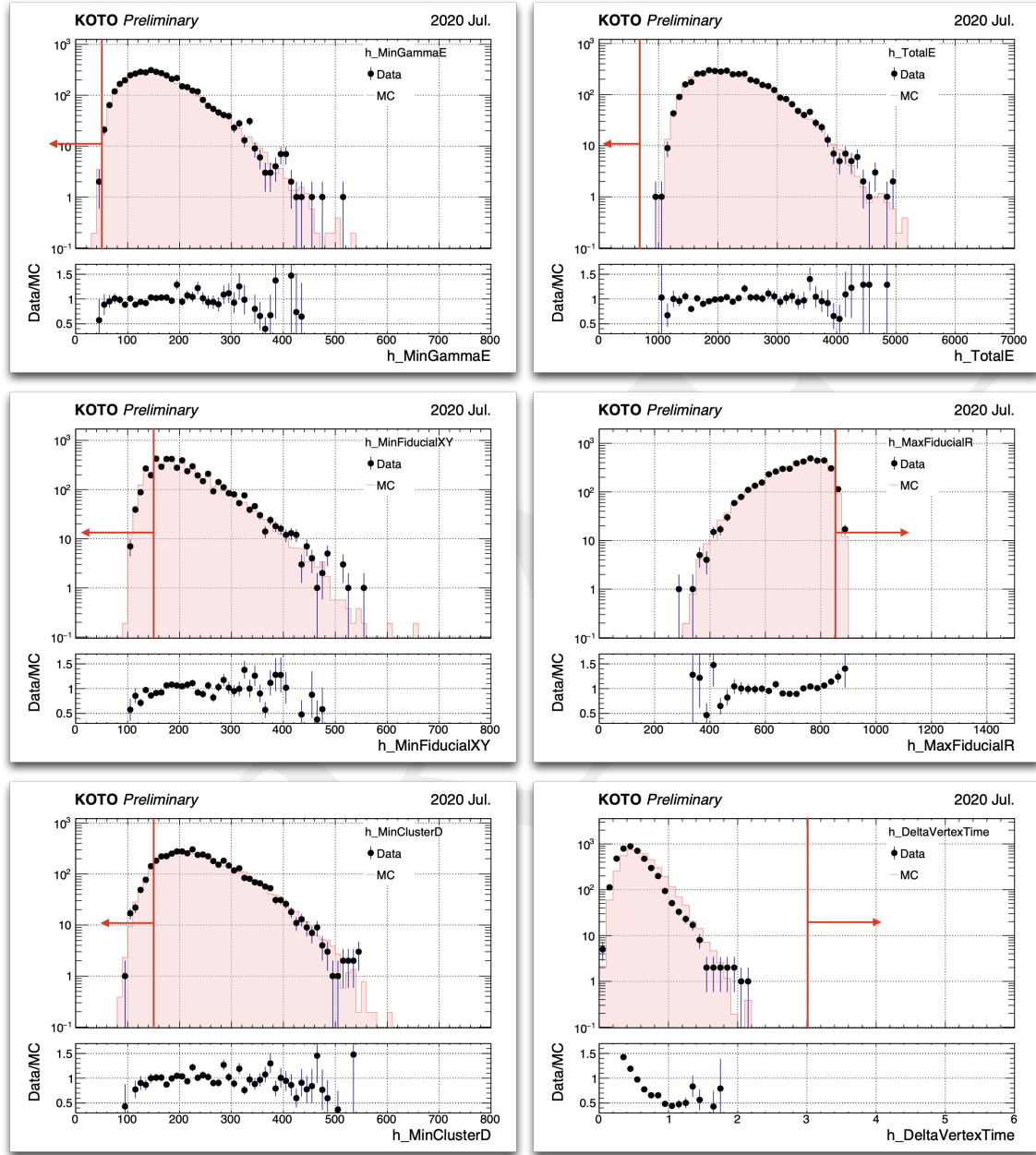


FIGURE 5.6: Distribution of the kinematic variables for the $K_L^0 \rightarrow 3\pi^0$ decay. All the selections are applied except the variable shown in the plot. The black point shows the data, and the fill histogram shows the Monte Carlo simulation. The red arrow indicates the cut-off value of the variable.

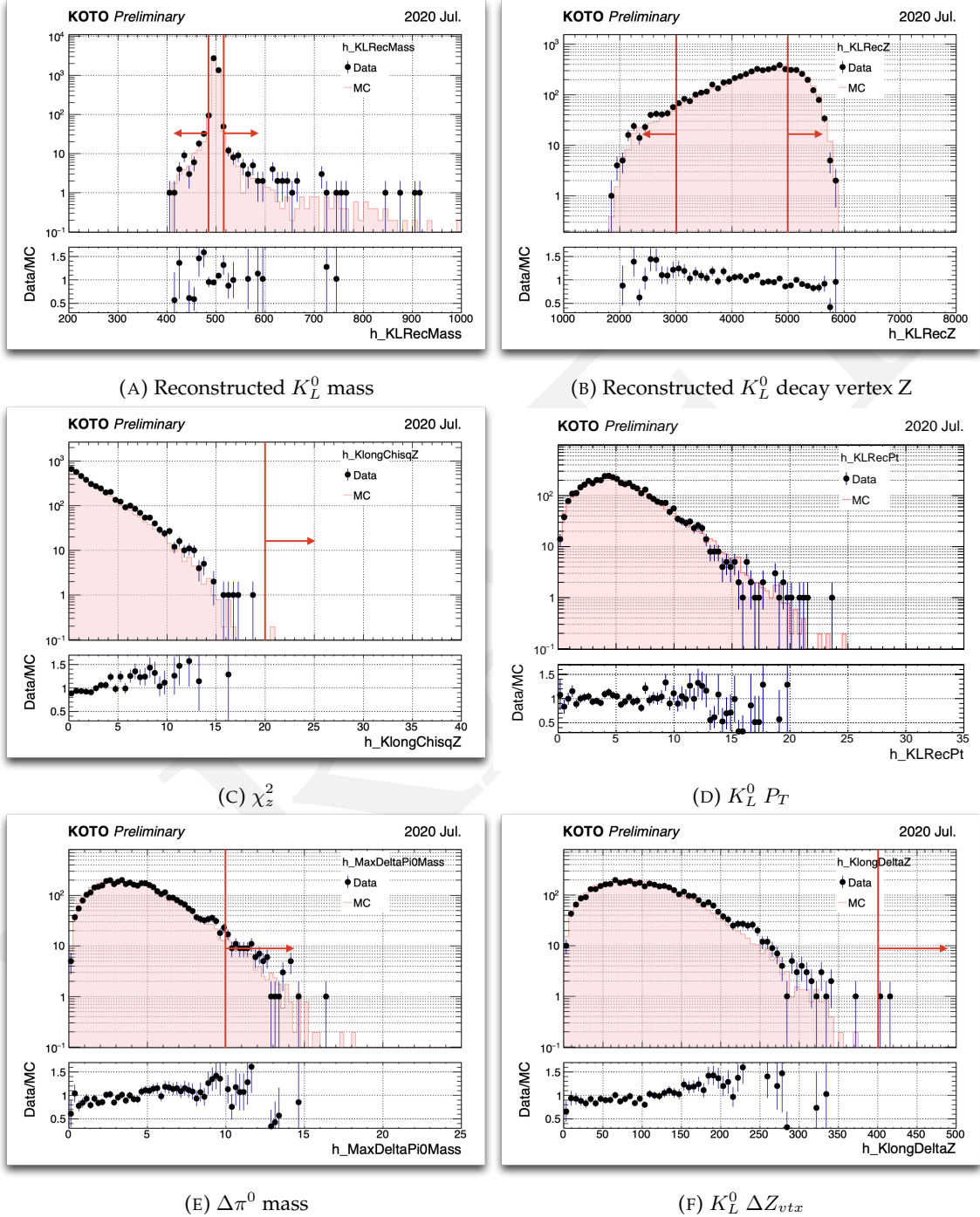


FIGURE 5.7: Distribution of the kinematic variables for the $K_L^0 \rightarrow 3\pi^0$ decay. All the selections are applied except the variable shown in the plot. The black point shows the data, and the fill histogram shows the Monte Carlo simulation. The red arrow indicates the cut-off value of the variable.

⁶⁷⁷ **Chapter 6**

⁶⁷⁸ **Analysis of $K_L \rightarrow \gamma\bar{\gamma}$**

⁶⁷⁹ The goal of the $K_L^0 \rightarrow \gamma\bar{\gamma}$ analysis is to estimate the branching ratio (\mathcal{BR}) of this decay,
⁶⁸⁰ we took a 2-hour special run with a single cluster trigger in 2020. The distinctive signal
⁶⁸¹ signature of $K_L^0 \rightarrow \gamma\bar{\gamma}$ manifests as a singular photon hit on the CsI calorimeter, devoid
⁶⁸² of any in-time hits on other detectors.

⁶⁸³ Employing a blind analysis method, we define a specific region, characterized by en-
⁶⁸⁴ ergy deposition $800 \text{ MeV} < E_\gamma < 3000 \text{ MeV}$ and a spatial constraint of $300 \text{ mm} < H_{XY}$
⁶⁸⁵ $< 850 \text{ mm}$, where H_{XY} denotes the maximum distance between the hit location and the
⁶⁸⁶ center of the CsI crystal along the x and y axes. The signal region has to be within the
⁶⁸⁷ blind region and has been optimized.

⁶⁸⁸ Our principal objective revolves around suppressing background noise and accentu-
⁶⁸⁹ ating signal events through event selection. Subsequently, we estimate the residual back-
⁶⁹⁰ ground events within the signal region post-selection. Under the assumption of negli-
⁶⁹¹ gible background noise, we calculate the Single Event Sensitivity (SES) to estimate the
⁶⁹² branching ratio upon observing signal events within the defined signal region. The SES,
⁶⁹³ representing the reciprocal of the product of the total K_L^0 yield and the acceptance of
⁶⁹⁴ signal decays, is expressed mathematically as:

$$SES = \frac{1}{Y \times A_{sig}} \quad (6.1)$$

⁶⁹⁵ Here, Y represents the K_L^0 yield, and A_{sig} signifies the signal acceptance. The branching
⁶⁹⁶ ratio (\mathcal{BR}) is then inferred from SES and the observed number of signal events (N_{sig})
⁶⁹⁷ within the signal region, as articulated by:

$$\mathcal{BR} = SES \times N_{sig} \quad (6.2)$$

⁶⁹⁸ However, when background contributions cannot be negligible, a statistical methodol-
⁶⁹⁹ ogy becomes imperative to ascertain the upper and lower bounds of signal event counts.
⁷⁰⁰ The background level (N_{bg}) is estimated through two approaches in this study. For K_L
⁷⁰¹ decay backgrounds, Monte Carlo simulations are employed to evaluate N_{bg} , defined by:

$$N_{bg} = Y \times \mathcal{BR}_{bg} \times A_{bg} \quad (6.3)$$

702 Where \mathcal{BR}_{bg} represents the branching ratio of specific background decays (e.g., $K_L \rightarrow$
 703 2γ), and A_{bg} denotes the acceptance corresponding to this background decay. For neu-
 704 tron backgrounds, a dedicated neutron data run is utilized, employing a data-driven
 705 approach for background-level evaluation through normalization against the neutron-
 706 dominant region between physics data and neutron data sample. Upon combining all
 707 background sources, a prediction of the background level within the signal region is de-
 708 termined. After an examination of reliability through the side-band region, uncover the
 709 blind region.

710 This chapter unfolds with a presentation of the event selection criteria, followed by
 711 a discussion on background suppression methodologies. Subsequently, the reliability
 712 of our analysis is assessed through a comparison between physics data and simulation
 713 results in the side-band region. The computation of background levels and SES is then
 714 detailed. With the final estimation in hand, we will proceed to open the box and the
 715 interpretation of the statistical result will be presented at the latest.

716 6.1 Data Set

717 As mentioned in the above section, for this analysis a special 2-hour run was taken in
 718 June 2020 (RUN85). In this special run, a single cluster trigger was adopted as the physics
 719 data, the energy threshold was set at 300 MeV with online veto and a pre-scale factor 1. To
 720 normalize this run, a normalization trigger is also accepted, this trigger does not contain
 721 the cluster number trigger, and only adopts CV as the online veto, with a pre-scale factor
 722 13. The POT of the 2-hour special is around 5.03×10^{-6} with the total 1.29×10^{10} number
 723 of K_L^0 enter KOTO detector, as shown in Chapter 5.

724 For the neutron background study, a neutron sample run was taken. As Section 4.7
 725 mentions, the GEANT4 MC toolkits cannot simulate the neutron interaction correctly,
 726 so the data-driven method was adopted to do the neutron background study. Ideally,
 727 for the single cluster study, a single cluster trigger neutron should be used in the study.
 728 Following this thought, a special single cluster Z0-Al run was taken in RUN85. However,
 729 after further study, we notice that the single cluster Z0-Al run cannot stand the neutron
 730 sample. Because we don't have a good method to purify the neutron event from the Z0
 731 data. Therefore, as a compromise, we use the 2-cluster trigger Z0 run in RUN85 which is
 732 taken for the $K_L^0 \rightarrow \pi^0 \nu\bar{\nu}$ decay study. The mechanism of the 2-cluster neutron event is
 733 that a neutron hits the CsI calorimeter and generates a new hadron through the hadronic
 734 interactions. Because there are two clusters on the CsI, the reconstruction was possible.
 735 Consequently, use the kinematic variable to select the neutron event, then a pure neutron
 736 sample data set was obtained. For the single cluster study, only the cluster with higher
 737 energy was selected because the primary neutron usually has higher energy than the
 738 second one.

Because the neutron flux is unable to be obtained, the background was normalized by the number of events in the neutron-dominated region in the neutron study. In this study, we adopt all Z0 data in RUN85, and the scale factor obtained by the normalization was around 1.6. This means the statistic of the neutron sample is far away to compare with physics data, it will behave on the statistical uncertainty.

6.2 Basic Strategy of the Single Cluster Study

6.2.1 Signal Identification

$K_L^0 \rightarrow \gamma\bar{\gamma}$ decay requires only one photon cluster to hit the CsI calorimeter and without any in-time hit in the rest of the detector. A single cluster can only provide the energy and position information. The lack of kinematic constraints will be the challenge of this study. Moreover, single cluster signatures are easily mimicked by some unknown arbitrary background. Requiring a high photon energy may help to suppress this kind of background but also reduce the signal efficiency.

6.2.2 Major Background Sources

The major background sources are K_L^0 decay background and neutron-like background.

K_L^0 decay background

Table 6.1 shows the main K_L^0 decay backgrounds. Other decay channels are unnecessary to be considered because of the low branching ratio. Only $K_L^0 \rightarrow \pi^\pm e^\mp \nu_e$ and $K_L^0 \rightarrow \pi^\pm \mu^\mp \nu_\mu$ are considered for the decay channel of charged particles in the final state, due to the high branching ratio. To suppress the K_L^0 decay background, studying these decay channels and understanding their characteristics are important. All of these decay channels produce more than one photon in the final state. Therefore, it is easy to suppress these decay channels with the KOTO detector. Except for the decay of $K_L^0 \rightarrow 2\gamma$, whose final state is similar to the signal signature and may be a potentially non-eliminable source of background.

TABLE 6.1: Main K_L^0 decay background modes and their branching ratios.

Decay mode	Branching Ratio
$K_L \rightarrow \pi^\pm e^\mp \nu_e$	$(40.55 \pm 0.11)\%$
$K_L \rightarrow \pi^\pm \mu^\mp \nu_\mu$	$(27.04 \pm 0.07)\%$
$K_L \rightarrow 3\pi^0$	$(19.52 \pm 0.12)\%$
$K_L \rightarrow \pi^+ \pi^- \pi^0$	$(12.54 \pm 0.05)\%$
$K_L \rightarrow 2\pi^0$	$(8.64 \pm 0.06) \times 10^{-4}$
$K_L \rightarrow 2\gamma$	$(5.47 \pm 0.04) \times 10^{-4}$

764 **Neutron-like background**

765 The neutron originating from the beamline poses a significant background challenge.
 766 Accurately simulating the in-beam neutron background is nearly impossible, especially
 767 without a defined mechanism to avoid it. The primary method to mitigate this back-
 768 ground involves distinguishing the cluster from the photon event.

769 **6.3 Single Cluster Event Selection**

770 The event selection included trigger cuts, kinematic cuts, and veto cuts. The trigger cuts
 771 were designed to mimic the online trigger effect, while the kinematic cuts and veto cuts
 772 were implemented to suppress background noise. The kinematic cuts were based on the
 773 reconstruction quantities of the photon cluster, while the veto cuts were just the criteria
 774 of hit on the veto counters. In the single cluster study, the signal significance of $K_L \rightarrow \gamma\bar{\gamma}$
 775 is only one photon cluster hit on the CsI calorimeter. And other vetoes keep silent in
 776 time. Which means a very loose condition for hitting events. It is also a challenge for this
 777 study.

778 **6.3.1 Trigger Selection**

779 The online trigger effect is the source of the difference between the collected data and the
 780 Monte Carlo simulation. To mimic the online trigger effect and ensure the consistency of
 781 the data and MC simulation, two trigger selections were implemented: the trigger timing
 782 cut and the total energy cut.

783 • **Timing window**

784 The online trigger will reject all events with any on-time veto hit, thus a trigger
 785 timing window as shown in Figure 6.1 is required to eliminate the online trigger
 786 effect. In the real data taking, due to the 8-ns clock dead time, the real physics data
 787 timing distribution will be wider than the Monte Carlo simulation. A wide enough
 788 timing window is selected to cover the distribution inconsistency between the data
 and the MC simulation.

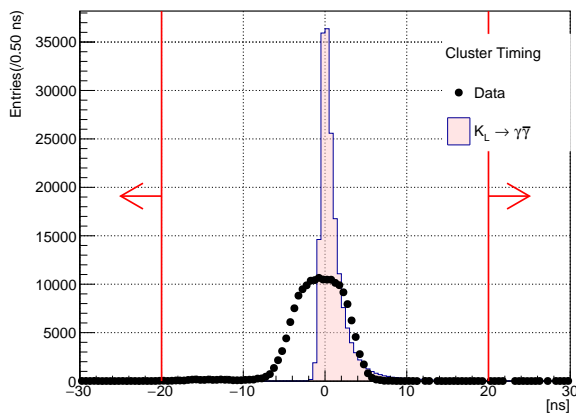


FIGURE 6.1: Distribution of cluster timing after relative timing correction. The dot is from real physics data, and the filled histogram is the MC simulation. The red arrow is the cut-off region.

789 • **Total Energy**

790 The offline energy cut should be larger than the online ET threshold to eliminate the
 791 online ET trigger effect. The online ET threshold of 300 MeV was required in the
 792 special run. Thus, the offline energy cut is set as 500 MeV. As shown in the Figure
 6.2, the signal acceptance is 91.0%

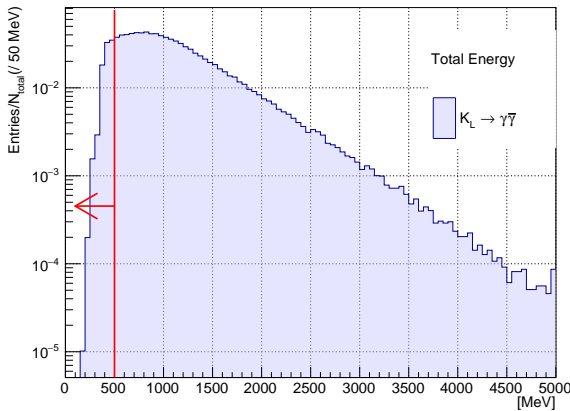


FIGURE 6.2: Distribution of total energy from Monte Carlo simulation. The histogram area is normalized to 1. The red arrow is the cut-off region.

793

794 **6.3.2 Kinematic Cuts**

795 The $K_L \rightarrow \gamma\bar{\gamma}$ decays require only one photon cluster on the CsI calorimeter. Therefore,
 796 the reconstruction of the mother particle is not possible, and also some variables based
 797 on multiple photon clusters will be absent, such as the vertex position, cluster distance,
 798 and KL kinematic quantities. As kinematic constraints are lacking, kinematic selection is
 799 determined by only two variables: the photon hit position and photon energy.

800 • **Innermost and Outermost Photon Hit Position**

801 To prevent the edge of the calorimeter from affecting cluster reconstruction, any
 802 event that hits the boundary will be removed. Based on the geometry of the calorime-
 803 ter, the outer boundary is evaluated using a radius of hit position, R_γ , while the
 804 inner boundary is evaluated using the maximum of the absolute values of x and y
 805 of the photon hit position, $\max\{|x_\gamma|, |y_\gamma|\}$. The inner boundary is set as a 300×300
 806 mm² box, while the outer boundary is a circle with a radius of 850 mm, as shown
 807 in Figure 6.3.

808 • **Photon energy**

809 Because of the 1 cluster study, the photon energy is almost equivalent to the total
 810 energy. Therefore, simply required photon energy to be larger than 500 MeV, which
 811 is the same as the total energy cut.

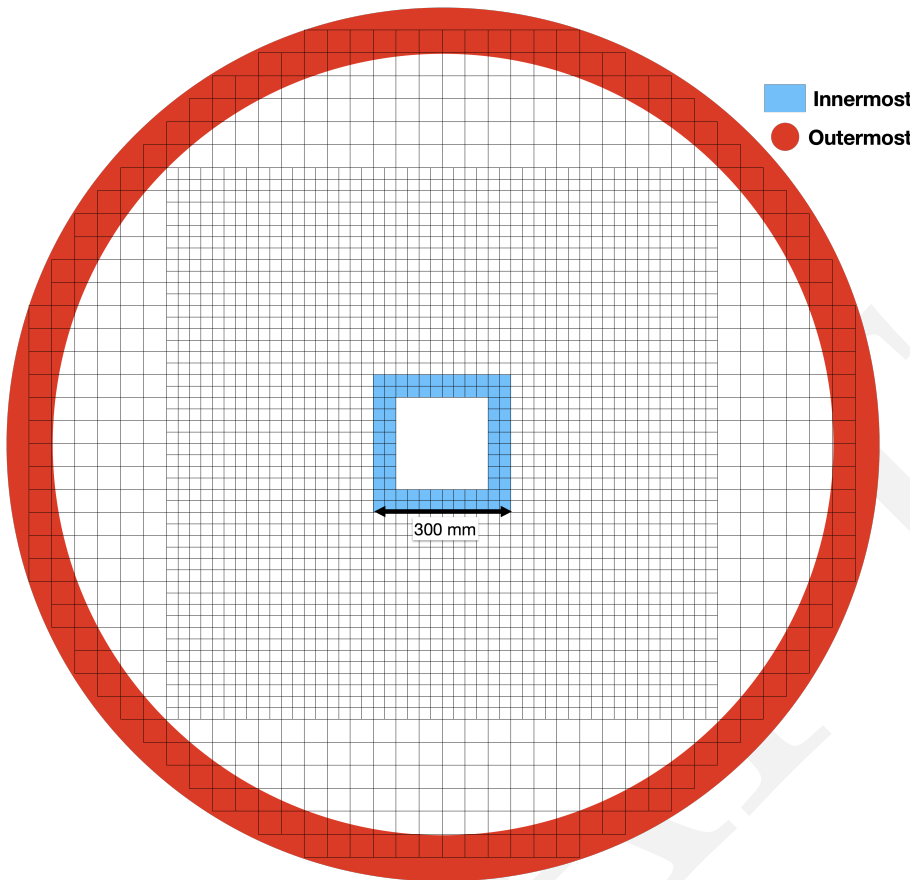


FIGURE 6.3: An upstream view of the CsI calorimeter. The red region is the outermost boundary, while the blue region is the innermost boundary.

6.3.3 Veto Cuts

Veto counters are the primary tool for Kaon decay background suppression in the KOTO experiment. The veto hits within the veto timing window and above the veto energy threshold will be tagged as an in-time veto hit. The event with any in-time veto hits will be treated as a background event and rejected. To determine a veto cut, the veto timing window and the energy threshold were required. The energy threshold was simply selected over the online veto and within the precision of the veto counter. The veto timing for veto hits is defined as talk in Section 3.4. To determine the reject window of the veto timing a timing study of each veto counter is required. First, the nominal timing should be determined, the hit close to the nominal timing should be considered as a background hit. Then determined the exact reject window of this veto, because the hit could be produced by the accidental hit not from the K_L^0 decay source. The window decision should consider the signal loss from the accidental hits.

In some veto counters, the source of the veto is predominantly the K_L^0 decay, which results in a Gaussian-like timing distribution, as an example shown in Figure 6.4. For these types of veto counters, the decision on the timing window is straightforward: it involves selecting a range of \pm a few nanoseconds around the peak position. The width

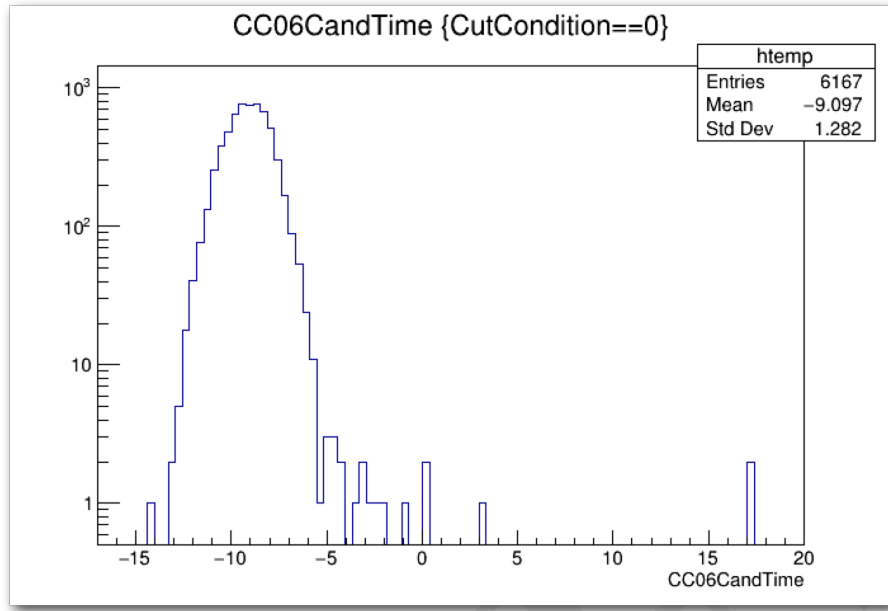


FIGURE 6.4: Distribution of veto timing of CC06.

829 of this window is determined based on the shape of the distribution.

830 However, in some veto counters especially for those surrounding the decay volume,
 831 the accidental hits are mixed with the background hit. In the following subsection, the
 832 veto study for these veto counters will be discussed.

833 FBAR and NCC

834 The veto timing is defined by the Equation 3.26 The FBAR and NCC are placed upstream
 835 of the decay volume, the distribution of timing is shown in Figure 6.5. The mechanisms
 836 of the hits can be categorized into these three types.

- 837 • **Upstream decays**

838 If a K_L^0 decays inside the FBAR chamber, the photon product can hit the FBAR or
 839 NCC, and the timing accumulated is the nominal time. In the Figure 6.5, is the event
 840 in decay vertex Z less than 2719 mm region. For NCC the veto timing in this region
 841 does not have a large variant which is because the K_L^0 decay before the NCC and
 842 the $(\Delta z - D)$ in Equation 3.26 is almost a constant and equivalent to the distance
 843 between NCC and CsI, regardless the decay position. However, because the K_L^0
 844 decays inside the FBAR, and it has a large volume, the $(Deltaz - D)$ will variant in
 845 a large range depending on the decay position.

846 In Figure 6.5, the veto timing of FBAR is broken into two peaks around the nominal
 847 time, which is because the NCC covers a part of the FBAR detector. In the Figure
 848 6.5a can show the agreement.

849 • **Backward hit**

850 When a K_L^0 decay in the decay volume, the photon could fly backward and hit the
 851 NCC and FBAR. Based on the Equation 3.26, the $(\Delta z - D)/c$ term will be a variant
 852 and the veto timing will depend on the decay vertex. However, the variate of this
 853 term is controllable,

$$\Delta z - D \approx \Delta z - (L - \Delta z) = 2\Delta z - L \quad (6.4)$$

$$T_{veto}(\Delta z) \approx \frac{2}{c}\Delta z + T_{mod} - T_{CsI} - L/c \quad (6.5)$$

854 where L represents the distance between veto and CsI. Equation 3.26 could be seen
 855 as a function to Δz with a slope $2/c$. Which explained the slope of the backward hit
 856 distribution in Figure 6.5a and 6.5b

857 • **CsI backsplash**

858 As shown in Figure 6.5a and 6.5b, a set of events with a veto timing independent
 859 of the decay vertex z . This phenomenon is called "backsplash" which is because the
 860 calorimeter did not consume all the EM shower but splashed upstream. Because
 861 the distance of the trajectory is constant, the veto timing will also be constant.

862 Based on these three mechanisms, only the CsI backsplash is the fake signal and the
 863 other two are the backgrounds. Therefore, the veto timing window for NCC and FBAR
 864 excludes the backsplash peak, as shown in Figure 6.5c and 6.5d.

865 **6.4 Background Suppression**

866 There are two main category background sources in this analysis: K_L decay events and
 867 Hadronic cluster. Besides these two main background sources, we will also discuss the
 868 other background sources that we study in this analysis, such as Charge Kaon decays,
 869 NCC background, and Halo Kaon backgrounds. In the following section, we will talk
 870 about the background suppression strategy for each category.

871 **6.4.1 K_L Decay Background**

872 In this analysis, we have studied the major three K_L^0 neutral decay channels, like $K_L^0 \rightarrow$
 873 $3\pi^0$, $K_L^0 \rightarrow \pi^0\pi^0$, and $K_L^0 \rightarrow 2\gamma$. And also the K_{e3}^0 , $K_{\mu 3}^0$, and $K_L^0 \rightarrow \pi^+\pi^-\pi^0$, which is the
 874 charge decay channel with a large branching ratio.

875 There are 3 kinds of possible mechanisms from K_L^0 decays were found:

876 • **Missing photon**

877 One photon hits the CsI, but other particles hit the dead material of the KOTO
 878 detector or missing in the beam hole.

879 • **Upstream decay**

880 K_L^0 decay upstream of the FBAR, one photon hits the CsI, and the other photon
 881 missing outside the detector.

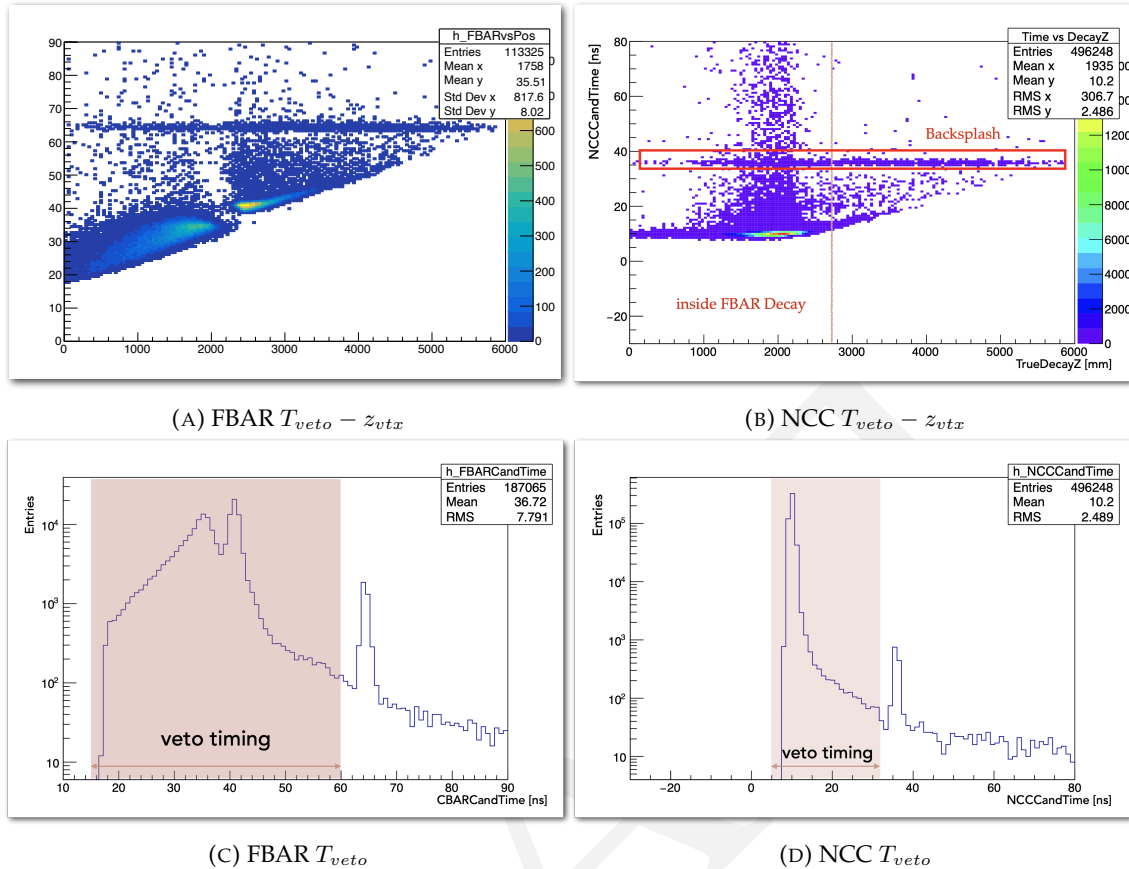


FIGURE 6.5: Temporary plots of FBAR and NCC

882 • **Fusion cluster**

883 The decay position along the Z-axis (Z_{vtx}) is too close to the CsI, all decay products
 884 hit the nearby crystal and are noted as a single cluster by the clustering process. As
 885 shown in Figure 6.8

886 In this section, all the studied K_L^0 backgrounds will be discussed. All the Monte Carlo
 887 simulations were applied the accidental overlay.

888 **$K_L^0 \rightarrow 2\gamma$ Background**

889 Because of the extreme hermetic of the KOTO detector, the possibility of missing multiple
 890 particles is very low. And with our powerful charge veto counter, it is also very difficult
 891 to miss a charged particle. Therefore, $K_L^0 \rightarrow 2\gamma$ decay with one missing photon will be
 892 the primary K_L^0 decay background in this study.

893 $K_L^0 \rightarrow 2\gamma$ background consists of two mechanisms, missing photon and upstream de-
 894 cay. $K_L^0 \rightarrow 2\gamma$ has very similar signature with the $K_L^0 \rightarrow \gamma\bar{\gamma}$, the only difference is another
 895 photon is visible. This means if the other photon of $K_L^0 \rightarrow 2\gamma$ is missing detecting, this
 896 event will be an ineliminable background in this study. The upstream decay mechanism
 897 is also having a missing photon. But its decay position is upstream of the FBAR, which

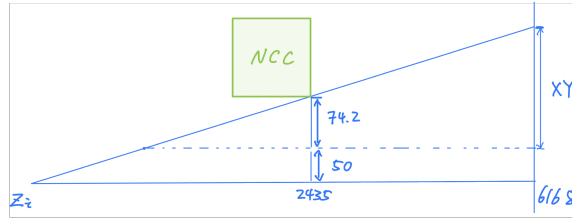


FIGURE 6.6: The schematic geometry diagram of the mechanism of the upstream decay background.

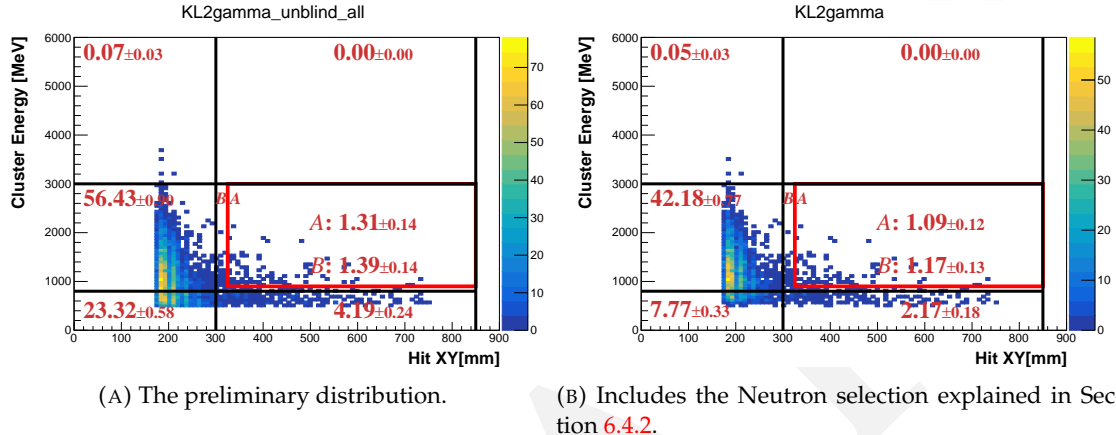


FIGURE 6.7: $E_\gamma - R_{XY}$ distributions of scattered $K_L^0 \rightarrow 2\gamma$ decays with various cut. The red frame indicates the signal region. The red number indicates the background level in each region.

898 highly constrains the hit radius (R_{XY}) of the cluster. Based on the geometry calculation
899 as shown in Figure 6.6, the maximum R_{XY} of the cluster of upstream decay is 265 mm,
900 which is outside the signal region.

901 Figure 6.7 shows the result of K_L^0 selection. A background level of 1.09 ± 0.12 is esti-
902 mated in the signal region.

903 Other K_L^0 decay Backgrounds

904 Besides the $K_L^0 \rightarrow 2\gamma$ background, the other K_L^0 decay backgrounds are also studied in
905 this analysis. Such as $K_L^0 \rightarrow 3\pi^0$, $K_L^0 \rightarrow \pi^0\pi^0$, K_{e3}^0 , $K_{\mu 3}^0$ and $K_L^0 \rightarrow \pi^+\pi^-\pi^0$. After the
906 event selection explained in Section 6.3 and 6.4.2, the event inside the signal region of all
907 decays except $K_L^0 \rightarrow 2\gamma$ is all rejected. All the three mechanisms mentioned above existed
908 in these decays. The missing photon is also an ineliminable background, but because the
909 decay products are much more than the $K_L^0 \rightarrow 2\gamma$, the missing photon background is
910 negligible. And the upstream decay background has the same geometry constraint as the
911 $K_L^0 \rightarrow 2\gamma$.

912 The fusion cluster mechanism is the most challenging one because the usual method
913 to reject this kind of background is to restrict the decay vertex Z (Z_{vtx}) position in a
914 reasonable region. However, in this study, the Z_{vtx} is not available due to the lack of

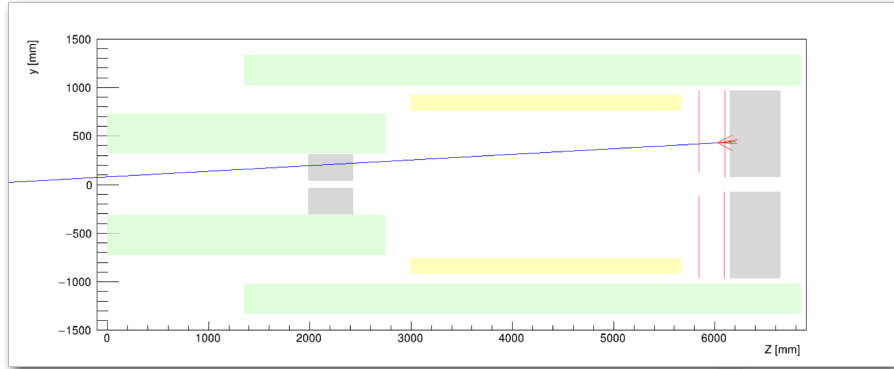


FIGURE 6.8: The schematic geometry diagram of the mechanism of the fusion cluster background.

915 kinematic variables. Therefore, we have to distinguish the fusion cluster from the single
916 cluster by the cluster shape.

917 The fusion cluster will have a wider shape than the single cluster because the fusion
918 cluster is the combination of two clusters. Which is more likely to be a hadronic-like clus-
919 ter. Thus, cluster shape discrimination with deep learning (CSDDL), which is explained
920 in Section 6.4.2, is sensitive to distinguish the fusion cluster from the single cluster.

921 If we assume the BR to be $\mathcal{O}(10^{-3})$, the number of signal events inside the signal region
922 is $\mathcal{O}(10^5)$. That means the Kaon decay background is negligible in this study.

923 Figure 6.9 shows the background level of other K_L^0 decays. The upper limit at 90%
924 confidence level is estimated in the signal region, as shown in Table 6.3.

925 6.4.2 Neutron Background

926 The in-beam neutron background is the dominant background in this study. The neutron
927 is generated by the hadronic interaction in the beamline, and it is called the "halo neutron"
928 also. The mechanism is that a neutron hits the CsI calorimeter with one cluster, and there
929 is no other in-time hit in the rest of the veto counters. Because the signature is the same as
930 the signal event, the regular background reject method can not reduce this background,
931 the neutron background is the most challenging in this study. Therefore, we developed
932 three techniques based on the $\gamma - n$ discrimination to suppress the neutron background.
933 The first and most powerful method is to discriminate the neutron cluster by the cluster
934 shape with deep learning. The second one is discriminating the neutron cluster by the
935 pulse shape difference with Fourier transformation. The last one is to use the both-end
936 readout system of CsI crystal to measure the shower depth of the cluster. These three
937 methods are explained in the following sections.

938 Cluster Shape Discrimination with Deep Learning(CSDDL)

939 The Cluster Shape Discrimination (CSD) method is based on the difference in the cluster
940 shape between the neutron event and the photon event. Because of the shower depth

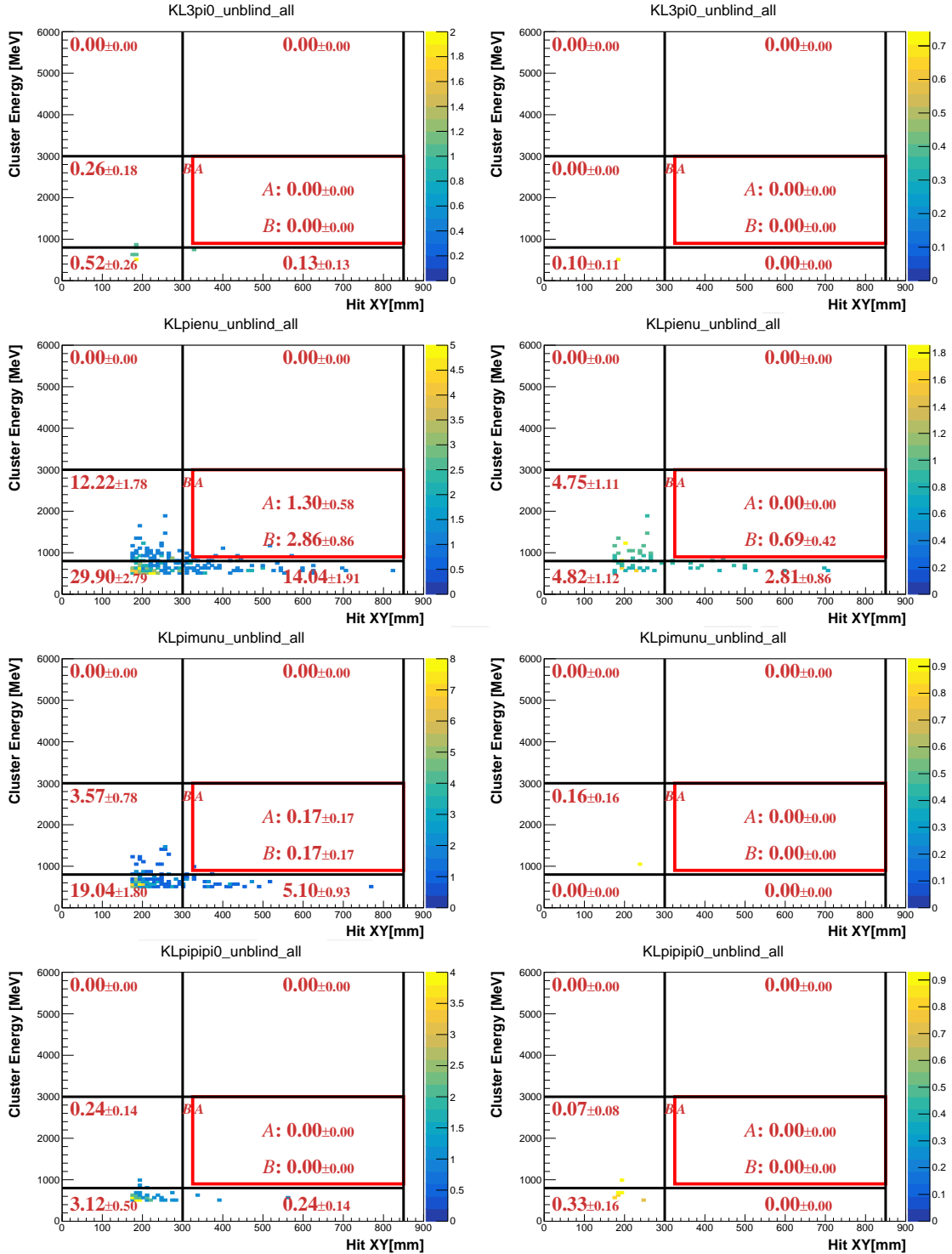


FIGURE 6.9: $E_\gamma - R_{XY}$ distributions of various background sources after applying all selection cuts. Left-hand side plots exclude the neutron cuts and the right-hand side plots include it. The red frame indicates the signal region. The red number indicates the background level in each region. (Region A indicates the Signal Region and Region B indicates the Blind Region excluding the signal region.)

difference, the neutron-like event will tend to be wider and shallower, and the photon-like event will be more narrow and depth, as shown in Figure 6.10. The difference is very easy to distinguish by the human eye, but it is very difficult to be quantified by the algorithm. Therefore, a neutral network model was developed to quantify the difference of the cluster shape difference.

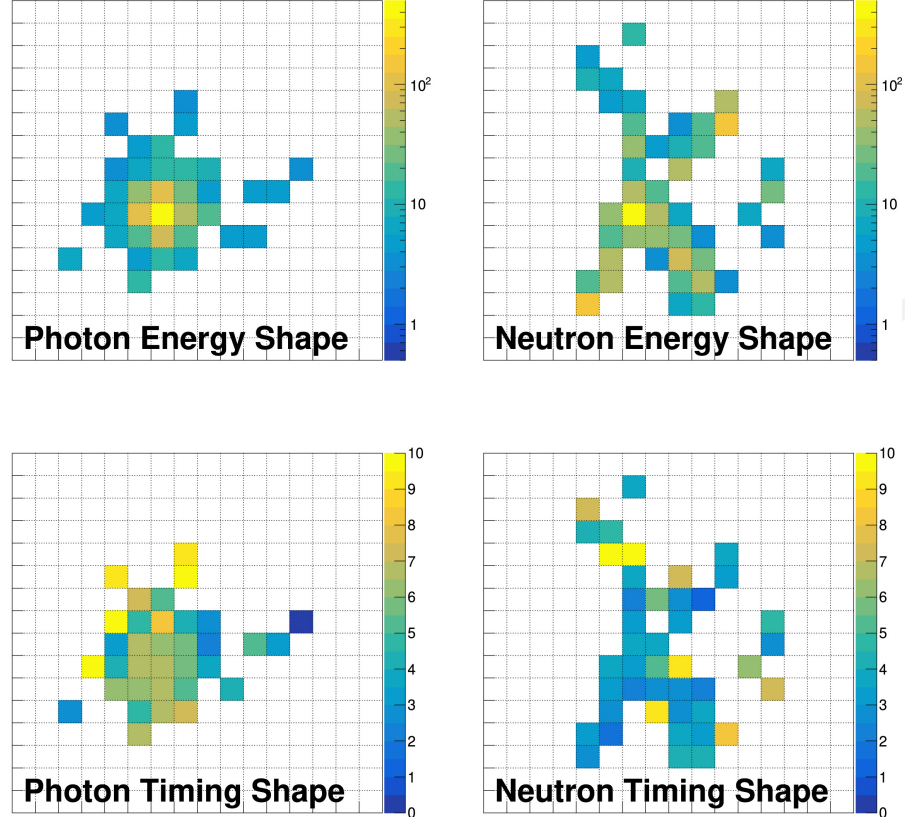


FIGURE 6.10: Example of the energy and timing shapes of photon cluster from the Monte Carlo simulation and neutron cluster from data. The color code represents the deposited energy in MeV and the timing in nanoseconds for each crystal in the cluster. [24]

In this study, the Convolutional Neural Network (CNN) architecture via TensorFlow was employed to classify the neutron and photon clusters by the energy and timing shapes [24]. We use the energy and timing for each crystal the cluster energy and the reconstructed angle on CsI (Φ) as the input parameter of the model training. The architecture of the CNN training process is shown in Figure 6.11.

The model was trained using a photon sample derived from Monte Carlo (MC) simulations and a neutron sample from actual experimental data. Specifically, the photon sample was sourced from the $K_L^0 \rightarrow \gamma\bar{\gamma}$ decay MC simulation, which includes accidental overlays. The choice of MC for the photon sample is crucial, as the training process relies on the precise measurement of energy and angle of clusters on the CsI detector, which are highly dependent on the assumed decay model. Utilizing a pure photon sample from experimental data, such as the 6-cluster events from $K_L^0 \rightarrow 3\pi^0$ decay, would risk overfitting the model to this specific decay configuration.

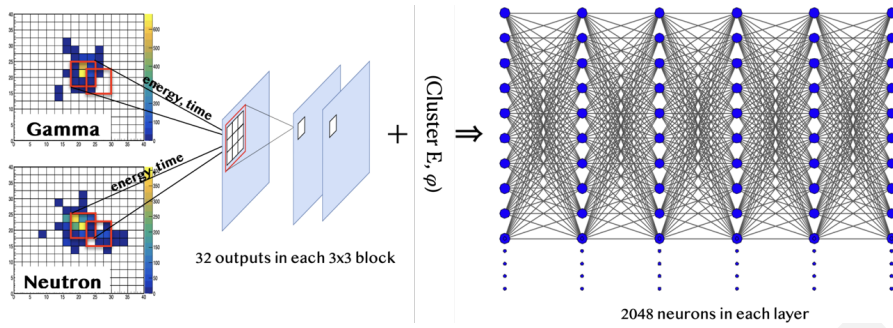


FIGURE 6.11: The architecture of CSD neural network training process.

For the neutron sample, we used data from the Z0-Aluminum (Z0-Al) runs, discussed in Section 4.7. It is important to note that the available Z0-Al data were insufficient for both analysis and training purposes. Consequently, we opted for a pragmatic approach by using data from the last Z0-Al run, specifically RUN82 from 2019, as our training dataset. To validate the suitability of the RUN82 neutron sample, we compared it against a smaller test set of neutrons from RUN85. This comparison, depicted in Figure 6.12, demonstrated a satisfactory alignment between the test results and the training dataset.

The performance of the CSD training result is illustrated by the acceptance of photon clusters in comparison to the rejection of neutron clusters on the CSD score, as shown in Figure 6.12. This training result gives a very high neutron rejection with high photon acceptance. A selection cut point was decided at a CSDDL score larger than 0.984 based on the 90% signal acceptance. At this point, the inefficiency of the neutron sample is up to $\mathcal{O}(-3)$

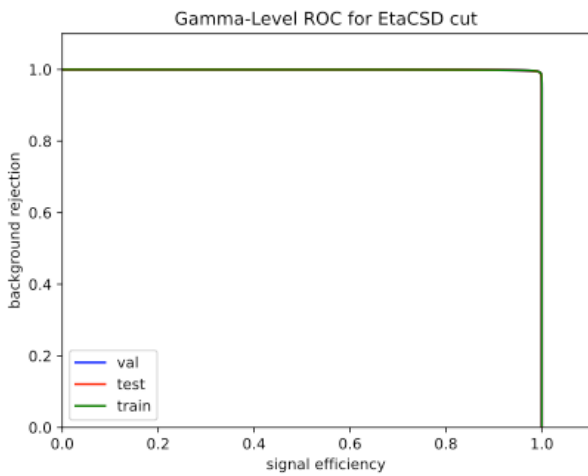


FIGURE 6.12: The ROC curve of the training model. The x-axis is the photon acceptance, and the y-axis is the neutron rejection.

Fourier transforms for Pulse shape discrimination (FPSD)

The difference in shower development of neutron and photon particles also manifests in the pulse shape difference in the CsI. The neutron pulses have a longer tail than the

975 photon sample because of the difference between the hadronic interaction and electro-
 976 magnetic interactions, as shown in Figure 6.13

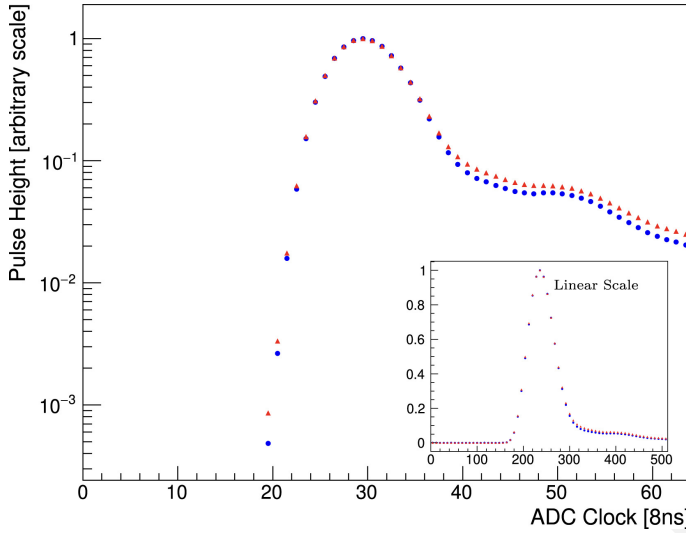


FIGURE 6.13: Average pulse shape of the neutron sample (blue dots) and photon sample (red dots) from one CsI crystal.[24]

977 The datasets for the neutron and photon samples were extracted from the data. The
 978 photon dataset is obtained from 6-cluster events, predominantly from the $K_L^0 \rightarrow 3\pi^0$
 979 decay. The neutron sample, utilized in the CSDDL model testing, comes from the same
 980 dataset.

981 The FPSD technique is employed to differentiate between neutron and photon clusters
 982 by analyzing the shape of the ADC waveform. We applied the Discrete Fourier Trans-
 983 form (DFT) to the raw ADC pulses and subsequently identified distinguishing features
 984 between neutrons and photons in the frequency domain. Figure 6.14 illustrates the like-
 985 lihood ratio obtained from this analysis. By setting a threshold that achieves 90% signal
 986 acceptance, we attained a background rejection efficiency of 89.6% for neutron clusters.

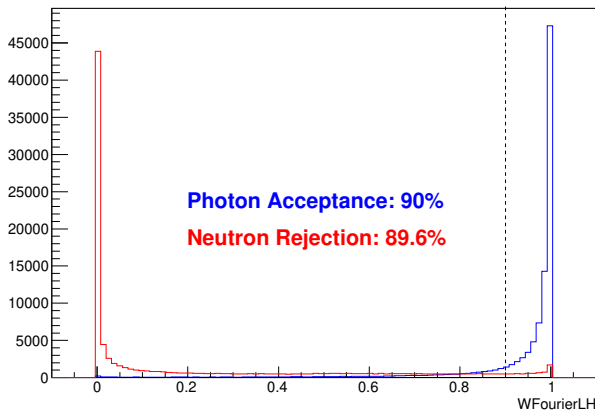


FIGURE 6.14: Distribution of the likelihood ratio for hadronic cluster events (red) and photon cluster events (blue). The photon cluster events are obtained through the $K_L^0 \rightarrow 3\pi^0$ decay analysis of data. The neutron sample is obtained from neutron data.

987 It is important to highlight that the FPSD algorithm relies on the CsI pulse shape,
 988 which is not incorporated in the MC simulations. Consequently, to implement this cut
 989 within the MC simulations, we utilize a table that outlines the FPSD cut efficiency. This
 990 table is structured based on the cluster energy, its position on the CsI detector, and the

991 specified cut value. When the FPSD is applied to an MC event, the algorithm searches
 992 for the corresponding cut efficiency in the table and applies this efficiency as a weighting
 993 factor to the event. This method ensures that the impact of the FPSD cut is accurately
 994 reflected in the simulation analysis.

995 **Shower-depth**

996 The radiation length for photons is shorter than the interaction length for neutrons, re-
 997 sulting in different shower depths in the calorimeter for photons and neutrons. Multi-
 998 pixel photon counters (MPPC) were installed in front of the CsI calorimeter, to consist of
 999 the both-end readout system with PMT. As shown in Figure 6.15, because of the shower
 1000 depth difference, the timing difference (ΔT) between the front-end (MPPC) and the back-
 1001 end (PMT) is different for the neutron and photon events. The ΔT (time difference) for
 1002 photon events tends to be smaller than that for neutron events.

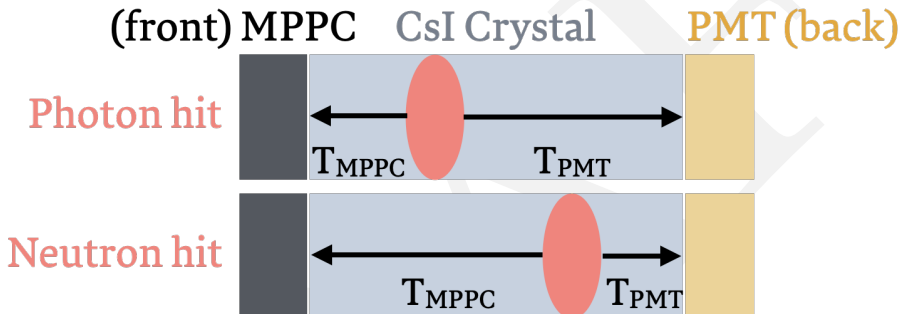


FIGURE 6.15: Illustration of shower depth means. An MPPC is installed on the upstream side. The time difference between the photon arriving upstream and downstream ($\Delta T = T_{MPPC} - T_{PMT}$) is used to measure the depth of the reaction and distinguish between photon events (up) and neutron events (down).

1003 The distribution of ΔT is shown in figure 6.16. By requiring ΔT to be less than 29.5
 1004 ns, the background rejection efficiency is 84% with a signal loss of 9%. The same data
 1005 described in Section 6.4.2 was used.

1006 **6.5 Single Event Sensitivity**

1007 After considering the 175 mm cut for the low-radius background and all the selection
 1008 cuts, the single event sensitivity (SES) is calculated by the equation 6.1. The SES is calcu-
 1009 lated by the K_L^0 yield and the signal acceptance. For this study, The K_L^0 yield is evaluated
 1010 by the $K_L^0 \rightarrow 3\pi^0$ decay, because the statistics of the 2-hour special physics data set are
 1011 not enough to evaluate the yield by $K_L^0 \rightarrow \pi^0\pi^0$ and $K_L^0 \rightarrow 2\gamma$ decays. After the selection
 1012 cuts in Section 5.2, no event will leave for the $K_L^0 \rightarrow \pi^0\pi^0$ and $K_L^0 \rightarrow 2\gamma$ decays. The
 1013 signal acceptance is evaluated by the Monte Carlo simulation with accidental overlay.
 1014 After applying all the selection cuts in Section 6.3, the signal acceptance is 2.66×10^{-3} .
 1015 And the K_L^0 yield is 1.29×10^{10} . The single event sensitivity (SES) is estimated to be
 1016 $(2.91 \pm 0.05_{stat.}) \times 10^{-8}$.

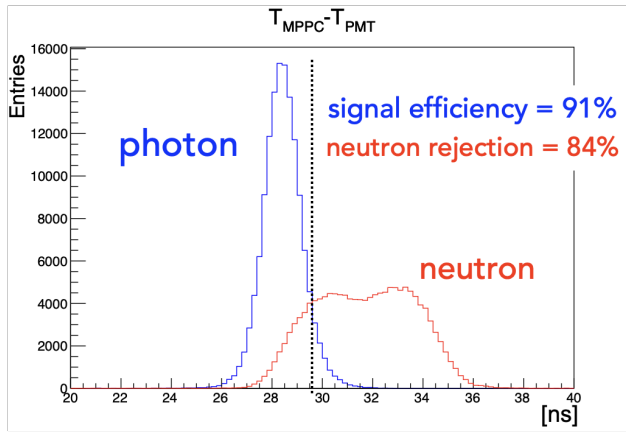


FIGURE 6.16: Distribution of the ΔT for neutron events and photon events. The photon cluster events are obtained through the $K_L^0 \rightarrow 3\pi^0$ decay analysis of data. The neutron sample is obtained by scattering neutrons in the beam with an Al plate.

$$SES = \frac{1}{Y \times A_{sig}} \quad (6.6)$$

$$= \frac{1}{1.29 \times 10^{10} \times 2.66 \times 10^{-3}} \quad (6.7)$$

$$= 2.91 \times 10^{-8} \quad (6.8)$$

1017 6.5.1 Systematic Uncertainty of SES

1018 Table 6.2 shows the summary of the systematic uncertainty from each source for the SES.

TABLE 6.2: Summary of Systematic Uncertainty for SES

Sources	Uncertainty
Veto Cuts	6.6%
Kinematic Cuts for $K_L^0 \rightarrow 3\pi^0$	3.3%
Kinematic Cuts for $K_L^0 \rightarrow \gamma\bar{\gamma}$	1.4%
Neutron Cuts for $K_L^0 \rightarrow \gamma\bar{\gamma}$	4.8%
K_L^0 momentum spectrum	0.9%
Trigger Effect	1.6%
Branching ratio of $K_L^0 \rightarrow 3\pi^0$	0.6%

1019 6.6 Additional Background Source Study

1020 After the event selection, there is a large discrepancy between the data and the simulation
 1021 in the low-radius region where $H_{XY} < 175$ mm. As shown in Figure 6.17, the data has
 1022 a higher level of background in the low-radius region than the simulation. To figure out
 1023 the contribution of this discrepancy, we studied some extra background sources. In the
 1024 following subsection, the description of these sources is shown.

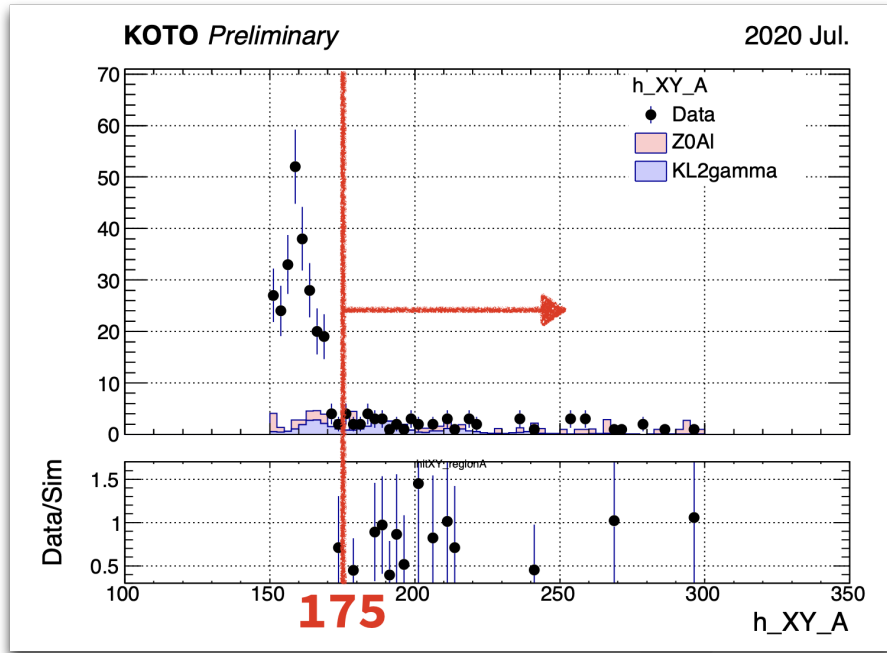


FIGURE 6.17: The R_{XY} distribution of the region 2. The red line and arrow indicated the cutoff region

1025 Upstream Decay from 2nd Collimator

1026 The discrepancy is centered at the region $R_{XY} < 175$ mm and the maximum R_{XY} of the
 1027 cluster of upstream decay is 265 mm, as Section 6.4.1 discussed. This means the upstream
 1028 decay is a very possible background source. Therefore, we extend the generated position
 1029 in the Monte Carlo simulation to the start of the 2nd collimator to study the very up-
 1030 stream decay background. In the usual simulation, the decay position is generated at
 1031 the end of the 2nd collimator, which is -1507 mm from the upstream of the FBAR. The
 1032 2nd collimator is 4 m long, which means the new decay position is -5507 mm from the
 1033 upstream of the FBAR. The geometry calculation, as Figure 6.6, shows that the maximum
 1034 R_{XY} of the cluster of the new decay position is 133 mm, which completely covers the
 1035 discrepancy region.

1036 The $K_L^0 \rightarrow 2\gamma$ decay was studied in this section. The normalization method is the
 1037 same as the usual Monte Carlo simulation but uses the upstream $K_L^0 \rightarrow 3\pi^0$ decay ($Z=-$
 1038 5507 mm) to estimate the K_L^0 yield.

1039 NCC background

1040 When a halo neutron hits NCC, a π^0 might be produced by the hadronic interaction. The
 1041 π^0 will decay to two photons and if one of them missing due to the inefficiency of the
 1042 detector, it will become a background source.

1043 **Charge Kaon Decay**

1044 As shown in Figure 4.1, though it is not a large amount, the charge Kaon remains in the
 1045 beamline.

1046 **Halo K_L^0 Background**

1047 Halo K_L^0 is the K_L^0 particles that are in the periphery of the beam core. As mentioned in
 1048 Section 4.4.2, the empirical K_L^0 spectrum does not consider the halo K_L^0 . The beamline
 1049 simulation was required to simulate the halo K_L^0 .

1050 **Summary of the Study**

1051 After the above extra background source study, the discrepancy in the low radius region
 1052 still exists. Currently, there are no further ideas for the search strategy. It is also possible
 1053 that just from upstream accidentally hit which is almost impossible to prob because the
 1054 sources are unknown and unclear. To handle is problem, we simply enlarge the inner-
 1055 most fiducial cut from 150 mm to 175 mm.

1056 **6.7 Background Level Estimation**

1057 Table 6.3 shows the background level of each background source in the signal region. The
 1058 upper limit at 90% confidence level is estimated in the signal region.

TABLE 6.3: Number of events predicted for each source inside the signal region

Source		Number of events
K_L decay	$K_L \rightarrow 2\gamma$	1.09 ± 0.12
	$K_L \rightarrow 3\pi^0$	< 0.18 (90% C.L.)
	$K_L \rightarrow 2\pi^0$	< 0.51 (90% C.L.)
	$K_L \rightarrow \pi^\pm e^\mp \nu_e$	< 0.27 (90% C.L.)
	$K_L \rightarrow \pi^\pm \mu^\mp \nu_\mu$	< 0.25 (90% C.L.)
	$K_L \rightarrow \pi^+ \pi^- \pi^0$	< 0.17 (90% C.L.)
Neutron		11.57 ± 4.42

1059 Figure 6.18 shows the E_γ - H_{XY} distribution of physics data for each region. In the
 1060 sideband region, the expected number shows agreement with the observations. The
 1061 background level in the signal region is 12.66 ± 4.42 .

1062 **6.8 Unbind the Signal Region**

1063 After all the studies, we decided to open the box. The observed result is 13 events inside
 1064 the signal region, as shown in Figure 6.19, which agrees with the expected number of
 1065 events. To estimate the Branching ratio of the $K_L^0 \rightarrow \gamma\bar{\gamma}$, the Feldman-Cousins method
 1066 was adopted, because we still have numerous expected backgrounds in the signal region.
 1067 After the calculation, an upper limit of branching ratio was obtained at 90% C.L.,

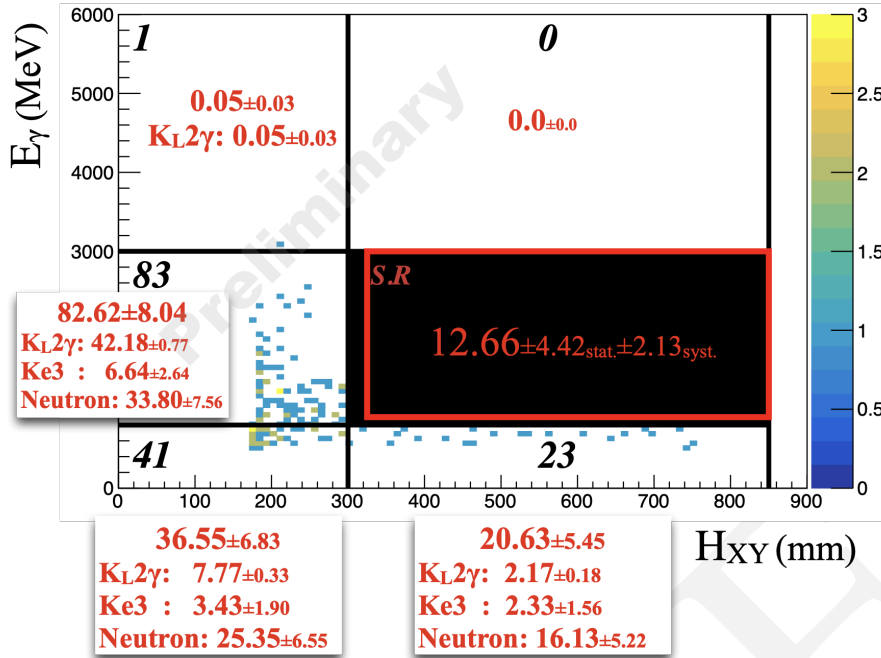


FIGURE 6.18: E_γ - H_{XY} distribution of physics data after applying all the selection cuts. The black box is the blind region the red frame is the signal region. The black (red) number is the observed (expected) number of events.

$$\mathcal{BR}(K_L^0 \rightarrow \gamma\bar{\gamma}) < 11.9 \times SES(K_L^0 \rightarrow \gamma\bar{\gamma}) \quad (6.9)$$

$$= 3.47 \times 10^{-7} (90\% \text{ C.L.}) \quad (6.10)$$

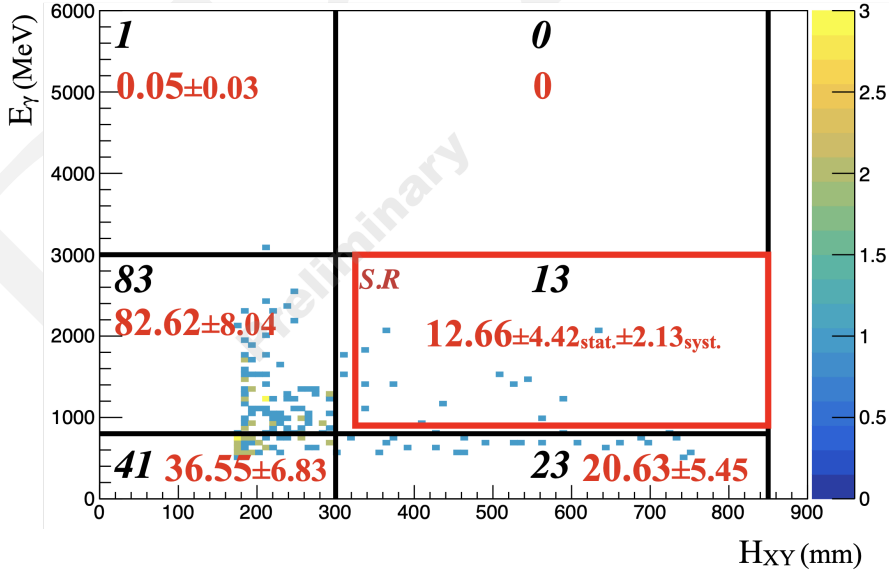


FIGURE 6.19: E_γ - H_{XY} distribution of physics data after open the blind box. The black (red) number is the observed (expected) number of events.

1068 **Chapter 7**

1069 **Conclusion and Discussion**

1070 We present the study of $K_L^0 \rightarrow \gamma\bar{\gamma}$ search in this thesis. The $K_L^0 \rightarrow \gamma\bar{\gamma}$ analysis is based
1071 on the 2-hour spacial run taken in 2020. The total number of K_L^0 decays is 1.29×10^{10} ,
1072 which is estimated by the $K_L^0 \rightarrow 3\pi^0$ decay. Two kinds of backgrounds are major in
1073 this analysis, the K_L^0 decay background and the in-beam neutron background. We use
1074 different methods to suppress these two backgrounds.

1075 To suppress the K_L^0 decay source background, we use the veto system of the KOTO
1076 detector. Because the one cluster signal signature is a pretty strict criterion to reject most
1077 of the K_L^0 decay channel with multiple products in the final state. The only background
1078 that can pass the veto system is the $K_L^0 \rightarrow 2\gamma$ channel. With one photon missing due to
1079 detection inefficiency, the $K_L^0 \rightarrow 2\gamma$ background cannot be rejected. Thanks to the her-
1080 metric veto system of the KOTO Experiment, the $K_L^0 \rightarrow 2\gamma$ background is well suppressed
1081 by the veto system with only $1.09 \pm 0.12_{stat.} \pm 0.05_{syst.}$ events estimated remaining in the
1082 signal region.

1083 To suppress the in-beam neutron background, we use three techniques based on the
1084 $n - \gamma$ discrimination to suppress the neutron background. The first one is cluster shape
1085 discrimination based on deep learning, which is the most powerful technique to classify
1086 neutrons and photons. The other two are the pulse shape discrimination based on the
1087 Fourier Transform and the show-depth measure by the CsI both-end readout system.
1088 These two techniques also provide a good rejection power on the neutron background.
1089 Combining these three techniques, rejected the neutron background by $\mathcal{O}(10^{-3})$ for the
1090 single cluster with 83.9% signal acceptance. After all the selections, the total neutron
1091 background is estimated to be $11.57 \pm 4.42_{stat.} \pm 2.13_{syst.}$ events in the signal region.

1092 Combining all the background sources we have studied, the total background is esti-
1093 mated to be $12.66 \pm 4.42_{stat.} \pm 2.13_{syst.}$ events in the signal region. After the background
1094 suppression study, we open the blind region box. The observed events in the signal re-
1095 gion are 13 events, which is consistent with the background estimation. Because we still
1096 have a large estimation of the background in the signal region, we decided to use the
1097 Feldman-Cousins method to evaluate the upper limit on the $K_L^0 \rightarrow \gamma\bar{\gamma}$ branching ratio.
1098 At 90% C.L., the upper limit on the $K_L^0 \rightarrow \gamma\bar{\gamma}$ branching ratio is 3.47×10^{-7} .

1099 7.1 Discussion for Next Step

1100 To advance the $K_L^0 \rightarrow \gamma\bar{\gamma}$ search, the next crucial step is to enhance the sensitivity of
1101 the analysis. Given the large number of background events within the signal region,
1102 collecting more physics data is not an immediate priority. In the current study, the pri-
1103 mary background source is beam neutrons. Despite employing three techniques to sup-
1104 press this background, the neutron background remains significantly estimated in the
1105 signal region. Thus, increasing the effectiveness of neutron background suppression is
1106 paramount. Additionally, enhancing the statistical power of the analysis is vital. At
1107 present, the neutron background estimation is plagued by considerable statistical uncer-
1108 tainty.

1109 For the next step, I suggest utilizing previously collected data to enhance the statistics.
1110 Since we do not use or need the single-cluster Z0-Al data in the analysis, we can repur-
1111 pose the data we have already collected. Specifically, data taken before the 2020 RUN85,
1112 which includes both physics and Z0-Al data, can be utilized. For single-cluster physics
1113 data, we can use the normalization trigger in the physics data, which does not filter based
1114 on the number of clusters. For Z0-Al data, we can continue using the two-cluster Z0-Al
1115 data, consistent with our current strategy.

1116 7.2 Massive Dark Photon Search

1117 We finished the massless dark photon study, the massive dark photon should be also an
1118 interesting topic to study. In this study, the search strategy is not strict with the mass of
1119 the dark photon. Therefore, the massive dark photon search will use the same strategy as
1120 the massless dark photon search. The only need to change is the mass of the dark photon
1121 in the MC simulation. Figure 7.1 shows the Upper limit and signal acceptance of each
1122 mass of the dark photon.

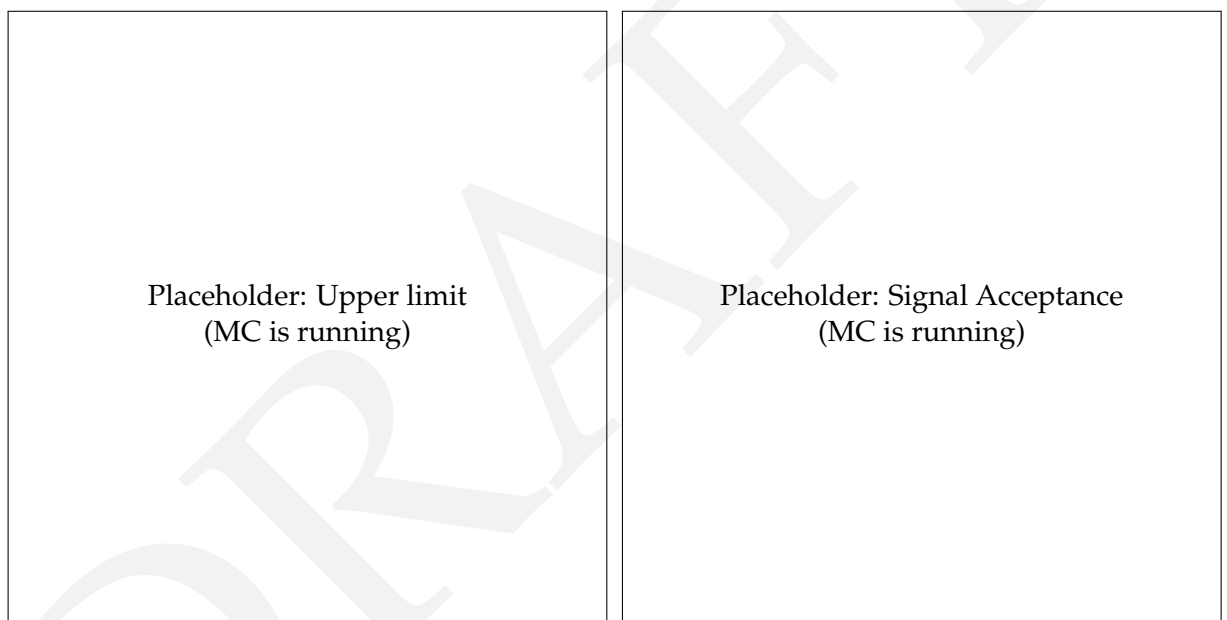


FIGURE 7.1: Upper limit (left) and signal acceptance (right) for each mass dark photon from 0 MeV to 250 MeV, step 25 MeV

¹¹²³ Bibliography

- ¹¹²⁴ [1] Particle Data Group et al. "Review of Particle Physics". In: *Progress of Theoretical*
¹¹²⁵ *and Experimental Physics* 2022.8 (Aug. 2022), p. 083C01. ISSN: 2050-3911. DOI: [10.1093/ptep/ptac097](https://doi.org/10.1093/ptep/ptac097).
- ¹¹²⁷ [2] Marco Fabbrichesi, Emidio Gabrielli, and Gaia Lanfranchi. *The Physics of the Dark*
¹¹²⁸ *Photon: A Primer*. Springer International Publishing, 2021. ISBN: 9783030625191.
¹¹²⁹ DOI: [10.1007/978-3-030-62519-1](https://doi.org/10.1007/978-3-030-62519-1).
- ¹¹³⁰ [3] Jhih-Ying Su and Jusak Tandean. "Kaon decays shedding light on massless dark
¹¹³¹ photons". In: *The European Physical Journal C* 80.9 (2020), p. 824. DOI: [10.1140/epjc/s10052-020-8338-3](https://doi.org/10.1140/epjc/s10052-020-8338-3).
- ¹¹³³ [4] Andrzej J. Buras et al. " $K^+ \rightarrow \pi^+ \nu \bar{\nu}$ and $K_L \rightarrow \pi^0 \nu \bar{\nu}$ in the Standard Model: status
¹¹³⁴ and perspectives". In: *Journal of High Energy Physics* 2015.11 (2015). DOI: [10.1007/jhep11\(2015\)033](https://doi.org/10.1007/jhep11(2015)033).
- ¹¹³⁶ [5] Shoji Nagamiya. "Introduction to J-PARC". In: *Progress of Theoretical and Experi-
¹¹³⁷ mental Physics* 2012.1 (Oct. 2012). 02B001. ISSN: 2050-3911. DOI: [10.1093/ptep/pts025](https://doi.org/10.1093/ptep/pts025).
- ¹¹³⁹ [6] Masanori Ikegami. "Beam commissioning and operation of the J-PARC linac". In:
¹¹⁴⁰ *Progress of Theoretical and Experimental Physics* 2012.1 (Sept. 2012). 02B002. ISSN:
¹¹⁴¹ 2050-3911. DOI: [10.1093/ptep/pts019](https://doi.org/10.1093/ptep/pts019).
- ¹¹⁴² [7] Hideaki Hotchi et al. "Beam commissioning and operation of the Japan Proton Ac-
¹¹⁴³ celerator Research Complex 3-GeV rapid cycling synchrotron". In: *Progress of The-
¹¹⁴⁴ oretical and Experimental Physics* 2012.1 (Sept. 2012). 02B003. ISSN: 2050-3911. DOI:
¹¹⁴⁵ [10.1093/ptep/pts021](https://doi.org/10.1093/ptep/pts021).
- ¹¹⁴⁶ [8] Tadashi Koseki et al. "Beam commissioning and operation of the J-PARC main ring
¹¹⁴⁷ synchrotron". In: *Progress of Theoretical and Experimental Physics* 2012.1 (Dec. 2012).
¹¹⁴⁸ 02B004. ISSN: 2050-3911. DOI: [10.1093/ptep/pts071](https://doi.org/10.1093/ptep/pts071).
- ¹¹⁴⁹ [9] Shunzo Kumano. "J-PARC Hadron Physics and Future Possibilities on Color Trans-
¹¹⁵⁰ parency". In: *Physics* 4 (May 2022), pp. 565–577. DOI: [10.3390/physics4020037](https://doi.org/10.3390/physics4020037).
- ¹¹⁵¹ [10] K. Takahashi H.and Agari et al. "Indirectly water-cooled production target at J-
¹¹⁵² PARC hadron facility". In: *Journal of Radioanalytical and Nuclear Chemistry* 305.3
¹¹⁵³ (2015), pp. 803–809. ISSN: 1588-2780. DOI: [10.1007/s10967-015-3940-9](https://doi.org/10.1007/s10967-015-3940-9).
- ¹¹⁵⁴ [11] T. Shimogawa. "Design of the neutral K0L beamline for the KOTO experiment". In:
¹¹⁵⁵ *Nuclear Instruments and Methods in Physics Research Section A: Accelerators, Spectrome-
¹¹⁵⁶ters, Detectors and Associated Equipment* 623.1 (2010). 1st International Conference on
¹¹⁵⁷ Technology and Instrumentation in Particle Physics, pp. 585–587. ISSN: 0168-9002.
¹¹⁵⁸ DOI: <https://doi.org/10.1016/j.nima.2010.03.078>.

- 1159 [12] D. Naito et al. "Development of a low-mass and high-efficiency charged-particle
 1160 detector". In: *Progress of Theoretical and Experimental Physics* 2016.2 (Feb. 2016). 023C01.
 1161 ISSN: 2050-3911. DOI: [10.1093/ptep/ptv191](https://doi.org/10.1093/ptep/ptv191).
- 1162 [13] Yosuke Maeda. *Charged-particle veto detector for the $K_L \rightarrow \pi^0\nu\bar{\nu}$ study in the J-PARC
 1163 K^0 TO experiment.* 2012.
- 1164 [14] Daichi Naito et al. "Evaluation of the Inefficiency of a Charged Particle Detector
 1165 for the KOTO Experiment". In: *JPS Conf. Proc.* 8 (2015), p. 024003. DOI: [10.7566/JPSCP.8.024003](https://doi.org/10.7566/JPSCP.8.024003).
- 1166 [15] C. Lin. "Study of $K_L^0 \rightarrow \pi^0\nu\bar{\nu}$ and $K_L^0 \rightarrow \pi^0\gamma\gamma$ with the Cluster-Finding Trigger at
 1167 KOTO". National Taiwan University, 2021. DOI: [10.6342/NTU202102308](https://doi.org/10.6342/NTU202102308).
- 1168 [16] Chieh Lin. "Data-Acquisition System Upgrade for the KOTO Experiment". In: *PoS
 1169 ICHEP2022* (2022), p. 242. DOI: [10.22323/1.414.0242](https://doi.org/10.22323/1.414.0242).
- 1170 [17] E. Iwai et al. "Performance study of a prototype pure CsI calorimeter for the KOTO
 1171 experiment". In: *Nuclear Instruments and Methods in Physics Research Section A: Accelerators,
 1172 Spectrometers, Detectors and Associated Equipment* 786 (2015), pp. 135–141.
 1173 ISSN: 0168-9002. DOI: <https://doi.org/10.1016/j.nima.2015.02.046>.
- 1174 [18] J. Allison et al. "Geant4 developments and applications". In: *IEEE Transactions on
 1175 Nuclear Science* 53.1 (2006), pp. 270–278. DOI: [10.1109/TNS.2006.869826](https://doi.org/10.1109/TNS.2006.869826).
- 1176 [19] S. Agostinelli et al. "Geant4—a simulation toolkit". In: *Nuclear Instruments and Methods
 1177 in Physics Research Section A: Accelerators, Spectrometers, Detectors and Associated
 1178 Equipment* 506.3 (2003), pp. 250–303. ISSN: 0168-9002. DOI: [https://doi.org/10.1016/S0168-9002\(03\)01368-8](https://doi.org/10.1016/S0168-9002(03)01368-8).
- 1179 [20] J. Allison et al. "Recent developments in Geant4". In: *Nuclear Instruments and Methods
 1180 in Physics Research Section A: Accelerators, Spectrometers, Detectors and Associated
 1181 Equipment* 835 (2016), pp. 186–225. ISSN: 0168-9002. DOI: <https://doi.org/10.1016/j.nima.2016.06.125>.
- 1182 [21] Kazufumi Sato. "Measurement of the CsI calorimeter performance and KL momentum
 1183 spectrum for the J-PARC KOTO experiment". Ph.D. thesis. Osaka University,
 1184 2015.
- 1185 [22] Particle Data Group et al. "Review of Particle Physics". In: *Progress of Theoretical and
 1186 Experimental Physics* 2020.8 (Aug. 2020). 083C01. ISSN: 2050-3911. DOI: [10.1093/ptep/ptaa104](https://doi.org/10.1093/ptep/ptaa104).
- 1187 [23] Kota Nakagiri. "Search for the Decay $K_L^0 \rightarrow \pi^0\nu\bar{\nu}$ at the J-PARC KOTO Experiment".
 1188 Ph.D. thesis. Kyoto University, 2019. DOI: [10.14989/doctor.k21564](https://doi.org/10.14989/doctor.k21564).
- 1189 [24] Y. C. Tung et al. "Suppression of neutron background using deep neural network
 1190 and Fourier frequency analysis at the KOTO experiment". In: *Nucl. Instrum. Meth.
 1191 A* 1059 (2024), p. 169010. DOI: [10.1016/j.nima.2023.169010](https://doi.org/10.1016/j.nima.2023.169010).
- 1192